NPS-OC-23-002

NAVAL POSTGRADUATE SCHOOL

MONTEREY, CALIFORNIA

Coupled Environment and Munition Burial and Movement (UnMUMB) Model for Assessing Characteristics of Munitions Underwater and Their Environment

Peter C. Chu

November 2023

Prepared for: The DoD Strategic Environmental Research and Development Program (SERDP), Munition Response (MR), Project MR19-C1-1073 (Final Report)

Page Intentionally Left Blank

This report was prepared under contract to the Department of Defense Strategic Environmental Research and Development Program (SERDP). The publication of this report does not indicate endorsement by the Department of Defense, nor should the contents be construed as reflecting the official policy or position of the Department of Defense. Reference herein to any specific commercial product, process, or service by trade name, trademark, manufacturer, or otherwise, does not necessarily constitute or imply its endorsement, recommendation, or favoring by the Department of Defense.

Page Intentionally Left Blank

REPORT DOCUMENTATION PAGE

1. REPORT DATE	2. REPORT TYPE	3. DATES COVERED	
		START DATE	END DATE
9/15/2023	Technical report	5/1/2019	3/1/2023

4. TITLE AND SUBTITLE

Coupled Environment and Munition Burial and Movement (UnMUMB) Model for Assessing Characteristics of Munitions Underwater and Their Environment

5a. CONTRACT NUMBER	5b. GRANT NUMBER	5c. PROGRAM ELEMENT NUMBER
	W74RDV90818446, W74RDV00801666	
5d. PROJECT NUMBER	**5e. TASK NUMBER**	**5f. WORK UNIT NUMBER**
MR19-C1-1073		

6. AUTHOR(S)

Peter C. Chu

7. PERFORMING ORGANIZATION NAME(S) AND ADDRESS(ES)	8. PERFORMING ORGANIZATION REPORT NUMBER
Naval Postgraduate School 1 University Circle Monterey, CA 93943-5000	NPS-OC-23-002

9. SPONSORING/MONITORING AGENCY NAME(S) AND ADDRESS(ES)	10. SPONSOR/MONITOR'S ACRONYM(S)	11. SPONSOR/MONITOR'S REPORT NUMBER(S)
Strategic Environmental Research and Development Program 4800 Mark Center Drive, Suite 17D03 Alexandria, VA 20003	SERDP	MR19-C1-1073

12. DISTRIBUTION/AVAILABILITY STATEMENT

Approved for public release: distribution unlimited.

13. SUPPLEMENTARY NOTES

14. ABSTRACT

The objectives of this project were: (i) to develop a model for underwater munition's mobility and burial (UnMUMB), (ii) to use SERDP field experimental data to explore seafloor environment characteristics such as liquefaction, sand wave migration and deep scour, (iii) to develop new methodology for deep scour burial, (iv) to use Delft3D to predict complex seafloor environment, (v) to develop a coupled Delft3D and wave induced liquefaction model to predict sandy seafloor morphological change, (vi) to develop a coupled Delft3D-UnMUMB model to predict under water munitions' mobility and burial as well as the change of the environment, and (vii) to provide the model formulations with User's Guide to SERDP investigators such as to whom working on a more sophisticated Underwater Munitions Expert System (UnMES) as well as to the larger SERDP, DoD, coastal engineering, and scientific communities via six peer-reviewed journal articles and the User's Guide for the coupled Delft3D-UnMUMB model.

15. SUBJECT TERMS

Prediction of Underwater Munitions' Mobility and Burial (UnMUMB), Delft3D, Coupled Delft3D-UnMUMB Model, Coupled Delft3D-Liquefaction Model, Deep Scour Burial, Sand Wave Migration

16. SECURITY CLASSIFICATION OF:			17. LIMITATION OF ABSTRACT	18. NUMBER OF PAGES
a. REPORT	b. ABSTRACT	C. THIS PAGE		
U	U	U	UU	71

19a. NAME OF RESPONSIBLE PERSON	19b. PHONE NUMBER *(Include area code)*
Peter C. Chu	(831) 656-3688

STANDARD FORM 298 (REV. 5/2020)
Prescribed by ANSI Std. Z39.18

Page Intentionally Left Blank

NAVAL POSTGRADUATE SCHOOL
Monterey, California 93943-5000

Ann E. Rondeau
President

Scott Gartner
Provost

The report entitled "Coupled Environment and Munition Burial and Movement (UnMUMB) Model for Assessing Characteristics of Munitions Underwater and Their Environment" was prepared for the DoD Strategic Environmental Research and Development Program (SERDP).

Approved for public release. Distribution is unlimited.

This report was prepared by:

CHU.PETER.CHENG.1230438176 Digitally signed by CHU.PETER.CHENG.1230438176 Date: 2023.11.13 07:49:43 -08'00'

Dr. Peter C. Chu
Distinguished Professor and Chair
Department of Oceanography

Reviewed by:

AMARA.JOMANA.H.1275843330 Digitally signed by AMARA.JOMANA.H.1275843330 Date: 2023.11.13 12:39:15 -08'00'

Dr. Jomana Amara
Vice Provost for Academic Leadership

Released by:

SMITH.KEVIN.B.1230026366 Digitally signed by SMITH.KEVIN.B.1230026366 Date: 2023.11.13 14:54:19 -08'00'

Dr. Kevin B. Smith
Vice Provost for Research

Page Intentionally Left Blank

Executive Summary

Many factors affect burial and mobility of munitions in underwater sedimentary environment. They are (a) physical and mechanical properties of the sediment, (b) fluid forces that act on the munition and the sediment in vicinity of the munition, (c) interaction between the munition and seabed (near field), and (d) far field bed dynamics of the coastal area of interest. The underwater environment is complex due to great nonlinear interacting processes and difficulty in reliable measurements. Prediction of burial and mobility is similar between underwater munitions and sea mines. The knowledge of sea mine's physical characteristics and understanding of its behavior under variety of sedimentary environments is most important, but still an inexact science. Observations show that burial is sensitive to the type of bottom sediment and nature of the fluid forcing, and the size and shape of the object. Mines planted in the areas of muddy sediments may sink upon impact.

During the ONR accelerated research initiative (ARI) "Mine Burial Prediction 2001-2005", a 6-DoF model was developed to predict three-dimensional trajectory of sea-mine through air, water, and sediment. This model contains full physics including nonlinear dynamics, fluid-structure interaction, instability theory, and bearing factor method to calculate the sediment force and torque with cavities for mine movements in sediment. On the base of Navy 's 6-DoF model, Delft3D, and field experiment data collected in SERDP MR-2320 (TREX13) and MR2319, an underwater munition mobility and burial (UnMUMB) model has been established in this project.

The project was formulated in direct response to the Statement of Need for the Munitions Response Program Area (MRSON-13-02), which called for topics that include (1) assessing and predicting the location of munitions relative to the seafloor, and (2) assessing the environment in which munitions are found. Furthermore, information obtained on munitions locations may be used to assess the utility of various underwater sensors and survey approaches.

The project enhances the ability to detect, classify, and remediate military munitions in aquatic environments such as estuaries, coastal and open ocean areas through development of a coupled ensemble sea-floor environment and UnMUMB model. The component for sea-floor environment is the well-known Delft3D (open source) to provide accurate map of the sediment type, seafloor morphology as well as accurate information of hydrodynamic conditions under atmospheric and tidal forcing. The component for munition 's mobility consists of an UnMUMB model. The coupled model is to provide statistically significant characteristics of munitions underwater and their environment.

The objective is to develop an effective coupled ensemble seafloor environment and UnMUMB model for the Munition Response (MR) community to assess the environment and to predict munitions' mobility. Since munitions' burial and mobility vary under various environment characteristics such as sediment types, sea floor morphology, and hydrodynamic conditions, timely prediction of seafloor environment and munitions' mobility including its location and burial is crucial to assess characteristics of munitions underwater and their environment.

The UnMUMB model uses the 6-DoF moment of momentum equation to predict underwater munition ‘s burial and mobility with various object parameters and initial conditions. The mobility is predicted by equation (13) and the burial is forecasted by equation (21). Delft3D output provides the environmental parameters around the munition, which are required by the UnMUMB model for predicting the munition’s burial and mobility. The capability of the coupled Delft3D-UnMUMB model was vilified using environmental conditions and spanning a range of object parameters reported in a separate study (MR-2320).

The surrogate and replica munitions’ mobility and burial were observed by divers and sector scanning sonar images during the field experiment depicted in Section 2 and in Calantoni et al. (2014). A total of 8 munitions in place at the shallow quadpod location were recovered by divers during the maintenance dive performed on 8 May 2013 (Figure 3b). Among 8 munitions, the 4 munitions with relative density (ρ_o/ρ_w) larger than 2.5, i.e., 3.11 (C4), 7.19 (C6), 2.72 (D3), and 7.19 (D6). The coupled UnMUMB-Delft3D model predicted no motion for C4 (ρ_o/ρ_w=3.11), C6 (ρ_o/ρ_w=7.19), D3 (ρ_o/ρ_w=2.72), and D6 (ρ_o/ρ_w=7.19); and mobility with displacement of 20.7 m for A2 (ρ_o/ρ_w=1.43), 6.52 m for C2 (ρ_o/ρ_w=1.20), 0.50 m for B5 (ρ_o/ρ_w=2.36), and 0.30 m for A5 (ρ_o/ρ_w=2.60). This may partially answer the question raised by Traykovski and Austin (2017) in a separate study (MR-2319): “For instance, would rapidly increasing waves be able to mobilize objects with relative densities greater than 2.5?”

Future work should explore the role to determine the threshold for mobility with objects near to or less dense than water-saturated sand tended to migrate, and denser objects tended to bury; and to identify munition ‘s migration distance under energetic wave and current forcing in environment with bathymetric constrained and with no bathymetric constrained. Besides, for operational use in the real world, the geometrical characteristics of objects need to be upgraded to include various shapes fitting the real munitions.

Table of Contents

List of Tables

List of Figures

List of Acronyms

ADCP	Acoustic Doppler Current Profiler
ADP	Acoustic Doppler Profiler
ADV	Acoustic Doppler Velocimeter
AST	Acoustic Surface Tracking
AWAC	An upward looking Nortek Acoustic Wave and Current Profiler
BSS	Brier Skill Score
CAD	Computer Aided Design
CESE6D	Coupled Ensemble Seafloor Environment and 6-DoF
DDB	Delft Dash Board
DoF	Degree of Freedom
ECMWF	European Centre for Medium-Range Weather Forecasts
ERA5	ECWMF Reanalysis within 5 Days of Real Time
JONSWAP	Joint North Sea Wave Project
KC	Keulegan-Carpenter
MOR	Morphology
MWL	Mean Water Level
NDBC	National Data Buoy Center
NOAA	National Oceanic and Atmospheric Administration
NGDC	National Geophysical Data Center
PC	Pulse Coherent
RMAE	Relative Mean Absolute Error
RMSE	Root Mean Squared Error
TREX	Target and Reverberation Experiment
MR	Munitions Response
TM	Technical Manual
UnMES	Underwater Munitions Expert System
UnMUMB	Underwater Munition Mobility and Burial
UXO	Unexploded Ordnance

Keywords

Underwater Munition Mobility and Burial (UnMUMB), UnMUMB model, Coupled Delft3D-UnMUMB model, Coupled Delft3D-Sediment Liquefaction Model, Riccati Equation, Sand Wave Migration, Keulegan-Carpenter (KC) number, Munitions' Shields Parameter, Sediment Shields Parameter.

Acknowledgements

Funding was provided by the Munitions Response program area of SERDP. We would like to thank Joseph Calantoni at the Naval Research Laboratory – Stennis Space Center and Alex Sheremet at the University of Florida for providing TREX13 data from SERDP Project 2320 and Peter Traykovski at the Woods Hole Oceanographic Institution for providing field experiment data from SERDP Project 2319 for environment assessment and model verification.

1. Abstract

1.1. Objectives

The objectives of this project were: (i) to develop a model for underwater munition ‘s mobility and burial (UnMUMB), (ii) to use SERDP field experimental data to explore seafloor environment characteristics such as liquefaction, sand wave migration and deep scour, (iii) to develop new methodology for deep scour burial, (iv) to use Delft3D to predict complex seafloor environment, (v) to develop a coupled Delft3D and wave induced liquefaction model to predict sandy seafloor morphological change, (vi) to develop a coupled Delft3D-UnMUMB model to predict under water munitions’ mobility and burial as well as the change of the environment, and (vii) to provide the model formulations with User’s Guide to SERDP investigators such as to whom working on a more sophisticated Underwater Munitions Expert System (UnMES) as well as to the larger SERDP, DoD, coastal engineering, and scientific communities.

1.2 . Technical Approach

We developed UnMUMB model (Chu 2020, 2022) on the base of the PI’s earlier efforts on establishing a 6-DoF model to predict three-dimensional trajectory of sea-mine through air, water, and sediment (Chu et al., 2004, 2005; Chu and Fan 2005, 2006, 2007; Chu 2009; Donas et al. 2021) for the ONR accelerated research initiative (ARI) “Mine Burial Prediction” during 2001-2005 (Bennett, 2000). This model contains full physics including nonlinear dynamics, fluid-structure interaction, instability theory (Chu and Fan 2005), and bearing factor method to calculate the sediment force and torque with cavities for mine movements in sediment (Chu and Fan 2007). We collaborated with SERDP funded efforts including MR-2319 “Continuous Monitoring of Mobility, Burial and Re-Exposure of Underwater Munitions in Energetic Near-Shore Environments”, MR-2320 “Long Time Series Measurements of Munitions Mobility in the Wave-Current Boundary Layer”, and MR19-1317 “Towards Developing Demonstrations for Munitions Mobility and Burial in the Underwater Environment” to get sufficient and reliable data in both seabed environment and munitions’ mobility/burial and MR19-1126 “Advanced Capabilities in the Underwater Munitions Expert System” to incorporate our effort into the Underwater Munitions Expert System (UnMES). We also obtained from identified and compiled through searches of academic journals, thesis and dissertation databases, DoD and NOAA reports, interlibrary loan, and the internet.

1.3. Results

Results were provided to the larger community via six peer-reviewed journal articles: Chu et al. (2022), which concentrated on development and verification of the UnMUMB model, Pessanha et al. (2022), which focused on sediment accretion in lower-energetic region, Pessanha et al. (2023a), which fixated on the wave-induced liquefaction, Passanha et al. (2023b), which focused on the sand wave migration, Gough et al. (2022), which established a new method for deep scour by an energetic wave event, Chu et al. (2021), which concentrated on development and verification of the coupled Delft3D-UnMUMB model. In addition, the User’s Guide for the Coupled Delft3D-UnMUMB model was published at the website: https://apps.dtic.mil/sti/citations/AD1173688.

2. Objective and SERDP Relevance

Our objective is to develop an effective coupled ensemble seafloor environment and UnMUMB model for the Munition Response (MR) community to assess the environment and to predict munitions' mobility. Since munitions' burial and mobility vary under various environment characteristics such as sediment types, sea floor morphology, and hydrodynamic conditions, timely prediction of seafloor environment and munitions' mobility including its location and burial is crucial to assess characteristics of munitions underwater and their environment.

Our project was formulated in direct response to the Statement of Need for the Munitions Response Program Area (MRSON-13-02), which called for topics that include (1) assessing and predicting the location of munitions relative to the seafloor, and (2) assessing the environment in which munitions are found. Furthermore, information obtained on munitions locations may be used to assess the utility of various underwater sensor and survey approaches.

Our project enhances the ability to detect, classify, and remediate military munitions in aquatic environments such as estuaries, coastal and open ocean areas through development of a coupled ensemble sea-floor environment and UnMUMB model. The component for sea-floor environment is the well-known Delft3D (open source) to provide accurate map of the sediment type, seafloor morphology as well as accurate information of hydrodynamic conditions under atmospheric and tidal forcing. The component for munition 's mobility consists of well-developed Navy 6-DoF model (Chu et al., 2004, 2005). The coupled model is to provide statistically significant characteristics of munitions underwater and their environment.

3. Background

Many factors affect the burial and mobility of munitions in underwater sedimentary environment. They are (a) physical and mechanical properties of the sediment, (b) fluid forces that act on the munition and the sediment in vicinity of the munition, (c) interaction between the munition and seabed (near field), and (d) far field bed dynamics of the coastal area of interest. Underwater environment is complex due to great nonlinear interacting processes and difficulty in reliable measurements. Prediction of burial and mobility is similar between underwater munitions and sea mines. The knowledge of sea mine's physical characteristics and understanding of its behavior under variety of sedimentary environments is most important, but still an inexact science (Taber 1999). Observations show that burial is sensitive to the type of bottom sediment and nature of the fluid forcing, and the size and shape of the object. Mines planted in the areas of muddy sediments may sink upon impact.

During the ONR accelerated research initiative (ARI) "Mine Burial Prediction" during 2001-2005 (Bennett, 2000), a 6-DoF model was developed to predict three-dimensional trajectory of sea-mine through air, water, and sediment (Chu et al., 2004, 2005; Chu and Fan 2006;

Chu 2009). This model contains full physics including nonlinear dynamics, fluid-structure interaction, instability theory (Chu and Fan 2005), and bearing factor method to calculate the sediment force and torque with cavities for mine movements in sediment (Chu and Fan 2007). On the base of Navy ‘s 6-DoF model, Delft3D, and field experiment data collected in SERDP MR-2320 (TREX13) and MR2319, an underwater munition mobility and burial (UnMUMB) model has been established.

3.1. Field Experiment Data from SERDP MR-2320 (TREX13)

Two types of data were analyzed for the UnMUMB and seabed modeling: (1) physical characteristics, mobility, and burial of munition surrogates and replicas, and (2) seabed environments such as currents, waves, and sediments. The data were obtained from a field experiment conducted in northern Gulf of Mexico near Panama City Florida sponsored by SERDP. Most information in this section can be found in Calantoni et al. (2014). Observations were collected from 21 April 2013 to 23 May 2013 to monitor the waves and currents while simultaneously tracking the location of surrogate munitions on the seafloor (Calantoni et al. 2014). The combined observations of munitions mobility and the driving hydrodynamic conditions will be used to validate predictions from the 6-DoF model to predict mobility and burial of seafloor cylindrical objects. During the field experiment, a range of surrogate munitions were deployed with variations in caliber, bulk density, shape, and rolling moment.

3.1.1. Munition Data

Four types of surrogate and replica munitions (Figure 1) that roughly represented the 155 mm HE M107, 81 mm mortar, 25 mm cartridge, and 20 mm cartridge were designed and fabricated using crude drawings and specifications provided by existing Army Technical Manuals (e.g., TM 43-0001-27 and TM 43-0001-28). Additional replica munitions for each of the four types listed above were purchased commercially (e.g., http://www.inertproducts.com/). The purchased replicas were used to provide overall dimensions and shape details for the four types of munitions. These purchased replicas were constructed from solid casts of urethane for the 155 mm and 81 mm calibers and solid aluminum for the 25 mm and 20 mm calibers (note the purchased 155 mm caliber was positively buoyant and not deployed).

A total of 4 surrogate munitions and 9 replicas were deployed at each of two water depths adjacent to the quadpod instrument frames (described below). Munition replicas have the general dimensions and shapes of their real counterparts with a single solid material to cover a range of bulk densities. Surrogate munitions are similar in size and shape to replicas except they were fabricated to have bulk densities and rolling moments that more closely match their real counterparts. The complete list of deployed and recovered objects along with brief descriptions and their material properties is given in Table 1. The mass for each object was determined post

fabrication prior to deployment. The density and rolling moment of munitions may be the most important munition ‘s characteristics affecting munition burial and mobility. The density listed for the replicas fabricated from a single solid material is the known material density. The volume and rolling moments for all objects were estimated using computer aided design (CAD) software. For the surrogates and replicas that are composites of more than one material the bulk density was estimated by combining the measured mass and the volume estimate from the CAD software.

Photos for the four types of surrogate munitions are shown in Figure 1. The first type was designed to represent the projectile, 155 mm, HE, M107, typically fired from 155 mm howitzers (left panels). The second type was designed to represent the 81 mm mortar (middle panels). The third and fourth types were designed to represent the cartridges, 25 mm and 20 mm (right panels). Each of the photos contains the fabricated surrogate, the purchased replica, and the replica fabricated from a single solid piece of aluminum (for 155 mm, bottom left), with a solid stainless steel body and aluminum tail section (for 81 mm, bottom middle), with a steel projectile fabricated with nearly identical density and dimensions to those found in the Army Technical Manual (for 25 mm and 20 mm cartridges, bottom right). The difference in rolling moment calculated for the 81 mm surrogate with and without fins is only 4.4%. While the fins seemingly add little to the total rolling moment, their interaction with the seafloor and bottom currents should not be underestimated. For 25 mm and 20 mm cartridges, a solid piece of Delrin plastic cut in the shape of the shell casing very closely matches the weight of the remaining portion of the munitions. Note that while a steel projectile is very common for the 20 mm type, we realize that the projectiles for the 25 mm type may be much more sophisticated and varied. Here we assumed the simplest solid steel projectile for the 25 mm type.

A combination of different acoustic Doppler current profilers (ADCPs) and acoustic Doppler velocimeters (ADVs), and pulse-coherent, acoustic Doppler profilers (PC-ADPs) were used to observe time series of the vertical profile of velocity at high spatial resolution near the bed and lower spatial resolution in the upper water column. Wave heights were obtained using both an acoustic surface tracking (Nortek AWAC) and pressure time series. Temperature, salinity, and pressure were also recorded near the bed. Finally, a sector scanning sonar was mounted on one of the legs of each of the quadpods, scanning a 110° swath every 12 minutes. The surrogate and replica munitions (described above) were deployed within the view field of the sector scanning sonar.

Instruments to observe the local hydrodynamics and resulting munitions mobility were mounted on a pair of large and rugged frames (herein referred to as “quadpods”) that were deployed at two different water depths (herein referred to as “deep” and “shallow”) during the Target and Reverberation Experiment (TREX13). The quadpods deployed in the northern Gulf of Mexico offshore of Panama City Beach, Florida USA (Figure 2). The deep quadpod was deployed at 30° 03.02330 N, 85° 41.33630 W in about 20 m water depth, while the shallow quadpod was deployed at 30° 04.80994 N, 85° 40.41064 W in about 7.5 m water depth.

Figure 1. Fabricated surrogate, purchased replica, and fabricated replica of (left) 155 mm HE M107, (middle) 81 mm mortar, and (right) 25mm and 20 mm cartridges (from Calantoni et al. 2014).

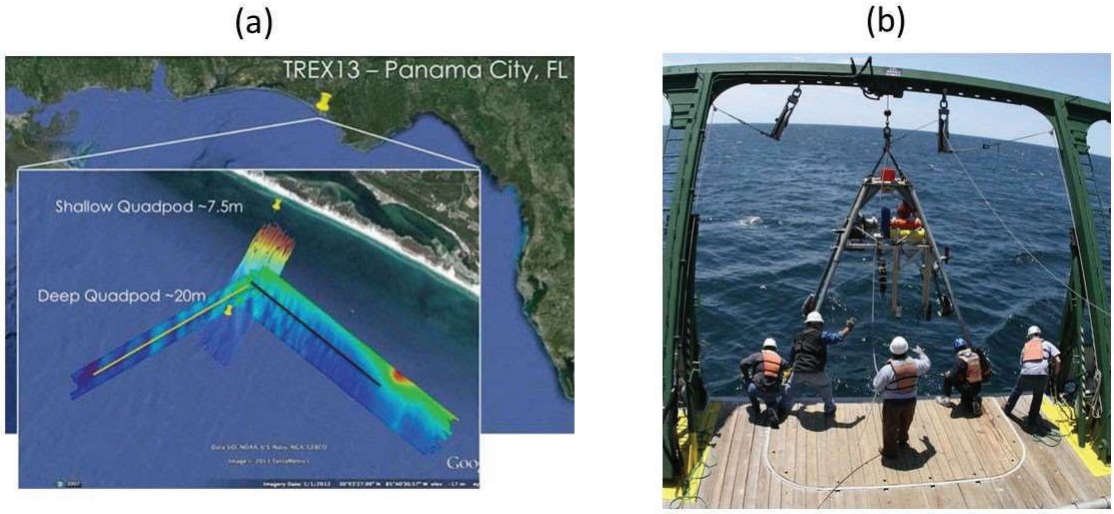

Figure 2. (a) Locations of deep and shallow quadpods, and (b) deployment of the deep quadpod (near 3.3 m tall) into around 20 m water depth from the R/V Smith around 12:40 (local time) on 20 April 2013 (from Calantoni et al. 2014)

Table 1. List of surrogate and replica munitions used during TREX13. A total of 26 objects were deployed and 18 objects were recovered (from Calantoni et al. 2014). Type surrogate munitions were fabricated to have rolling moments within 10% of the estimated rolling moment of the real counterpart.

Type	Labels	Materials	Type	Recovered	Volume (10^{-5} m^3)	Mass (kg)	Density (10^3 kg/m^3)	Rolling Moment (10^{-4} $kg\ m^2$)
155 mm, HE, M107	D5, D6	Delrin, 304 Stainless	Surrogate	D5, D6	768.38	34.15	4.444	923.59
	D3, D4	Aluminum	Replica	D3, D4	768.38	20.91	2.721	500.48
81 mm mortar	C3, C4	Delrin, 316 Stainless, Aluminum tail fins	Surrogate	C3, C4	120.93	3.76	3.109	24.73
	C5, C6	304 Stainless, Aluminum tail fins	Replica	C5, C6	120.93	8.70	7.194	50.51
	C1, C2	Urethane	Replica		120.93	1.45	1.199	8.34
25 mm cartridge	B5, B6	Delrin, 316 Stainless	Surrogate	B5, B6	16.55	0.39	2.356	0.46
	B7, B8	304 Stainless	Replica	B7, B8	16.55	1.32	7.976	1.98
	B3, B4	Aluminum	Replica	B3, B4	16.55	0.43	2.598	0.68
	B1, B2	Delrin	Replica		16.55	0.23	1.390	0.35
20 mm cartridge	A5, A6	Delrin, 316 Stainless	Surrogate	A6	7.70	0.20	2.597	0.13
	A7, A8	304 Stainless	Replica	A7	7.70	0.63	8.182	0.53
	A3, A4	Aluminum	Replica	A3, A4	7.70	0.19	2.468	0.18
	A1, A2	Delrin	Replica		7.70	0.11	1.429	0.09

Divers laid the surrogate and replica munitions on the seafloor around each quadpods according to a predetermined schematic (Figure 3a). The light blue arc roughly denotes the field of view of the sector scanning sonar. The dark blue circle in the upper left denotes the location of the surrogates. The other replicas were grouped according to relative bulk density. In this case the red boxes denote the objects that were not recovered from the shallow quadpod site. Observations during a maintenance dive (8 May 2013) immediately after the storm event (5-6 May 2013) suggest that the surrogates and replicas may have been buried in place as opposed to being transported away by the waves and currents (Figure 3b). Munitions mobility and burial for the largest surrogates and replicas deployed was observed at the shallow quadpod location in during the

passage of an atmospheric front (storm event), 5 – 6 May 2013. However, at the deep quadpod location at 20 m water depth during the same storm relative observed changes in the state of the surrogate and replica munitions were minimal. The 155 mm replica fabricated from solid aluminum was partially buried in the crest of a sand ripple. The sharp crest of the ripple (or bedform) is visible in the foreground of the image, indicated by the black arrow. The replica shown here was the only object not completely buried during the storm event at the shallow quadpod location (Figure 3c). Excavating by hand, divers were able to recover a total of 8 munitions buried just below the surface very near the known initial locations at the shallow quadpod during the maintenance dive performed on 8 May 2013.

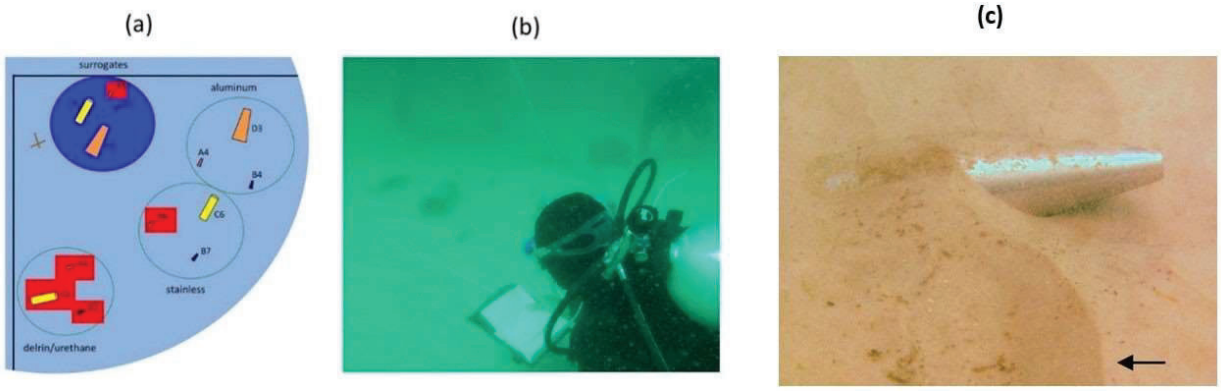

Figure 3. (a) The layout of objects laid by divers under the shallow quadpod (similar for deep quadpod), (b) the photo of divers laying the object field during the shallow quadpod deployment, and (c) the object field of the shallow quadpod taken on the morning of 8 May 2013 (from Calantoni et al. 2014).

3.1.2. Seafloor Evolution

Seafloor evolution before, during, and after the two wave events at the shallow quadpod location are presented in Figure 4. All sonar images were averaged in a time window of 4 hours centered on the date/time displayed in each image to reduce the noise. As previously reported by Pessanha et al. (2022), before the first wave event on 4 May 0600 2013 (Figure 4a), the sonar image shows sand ripples and three objects highlighted by the blue arrows. Two of these objects are 15.5 cm in diameter, while the third (near the center of the sonar image) is 8.1 cm. On 4 May 0900 (Figure 4b), the incoming swell associated with the first wave event stirred up the sediment, causing changes in the sand ripples. After the first wave event on 5 May 0600, the sonar image displays objects on the seafloor and indicates that the sediment accretion was not sufficient for the burial of objects (Figure 4c). The second wave event had a more extensive duration and impact on the seafloor. During the second wave event on 5 May 1900 and 6 May 0600 (Figures 4d and 4e), the bedform changed and the sand partially covered the objects. Eventually, the objects were completely buried, as shown in Figure 4f (7 May 0600). On 8 May, all objects near the shallow quadpod location were recovered during a maintenance dive, confirming the objects were buried and not mobilized by the flow.

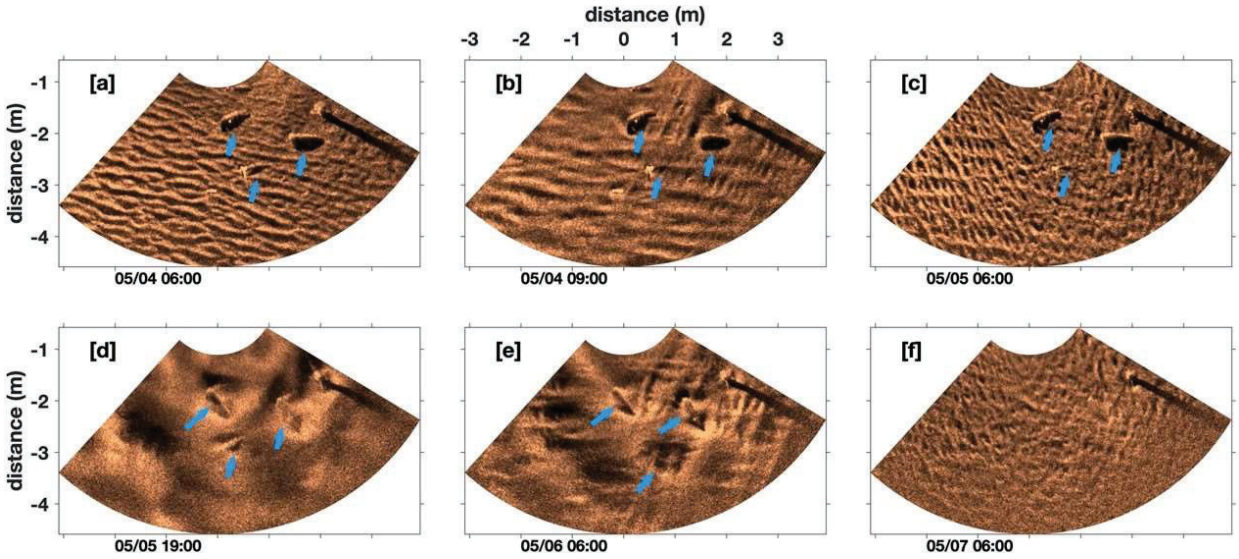

Figure 4. Sector scanning sonar images in 2013 on (a) 4 May 0600, (b) 4 May at 0900, (c) 5 May 0600, (d) 5 May 1900, (e) 6 May 0600, and (f) 7 May 0600. Sonar images show three objects (highlighted by the blue arrows) near the location of the shallow quadpod during TREX13 (from Pessanha et al. 2022).

3.2. Field Experiment Data from SERDP MR-2319

The data were collected in a region with strong tidal currents and intermittent energetic wave events at the Wasque Shoals, about 1 km from the southeastern corner of Martha's Vineyard, Massachusetts (Figure 5a). Most information in this section can be found in Traykovski &Austin (2017). It is characterized by a sandy seabed and tidal currents exceeding 1 m/s with direction predominantly east–northeast and west during the flood and ebb, respectively. Currents in this region are dominated by the M2 and N2 semidiurnal tidal currents, which are responsible for roughly 80% and 10% of the variance, respectively (Hopkins et al. 2017). Surface wave direction during the field experiment primarily ranges between south and southwest. Significant wave height decreases with decreasing water depth (Traykovski & Austin 2017). According to Hopkins et al. (2017), the ebb jet splits from the sharp shoreline around the southeastern corner of Martha's Vineyard, which reduces the ebb flow and creates an asymmetric flow pattern with a dominant flood. The complex bathymetry, with depth varying from 2 to 7 m, includes periodic bedforms such as mega ripples and sand waves. On the shoals, tidal sand wave heights range from 2 to 4 m (Traykovski & Austin, 2017).

A quadpod was deployed on 20 November 2013 (white square in Figure 5b shows its location (41.3404° N, 70.459° W)) in a water depth of approximately 6.5 m. A Nortek Aquadopp sensor was placed on the quadpod with 0.2 m vertical bin measured velocity over a range of 2 m, which were used to compute the hourly mean depth-averaged current velocity. Furthermore, significant wave height, mean wave direction, and peak wave period were estimated from pressure sensors of the acoustic Doppler velocimeters (ADVs) attached to the quadpod.

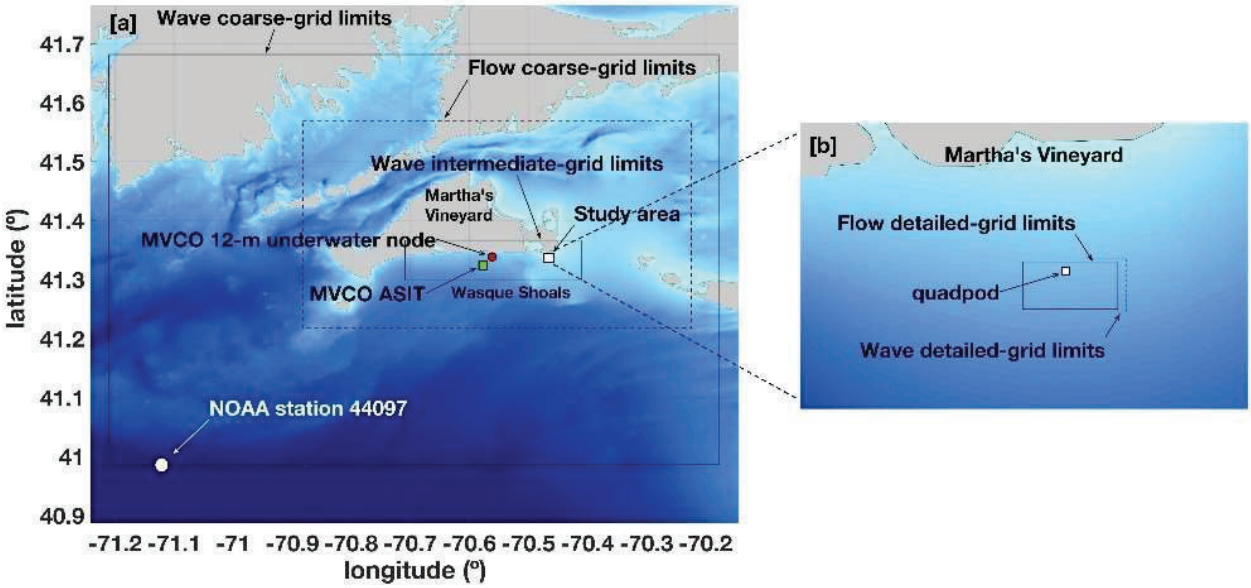

Figure 5. Study area and limits of model grids. (a) Wave coarse-grid area (thick solid lines), flow coarse-grid area (dashed lines), wave intermediate-grid area (thin solid lines) with the NOAA station 44097 represented by the white dot at the southern boundary of the wave coarse-grid area (40.967° N, 71.126° W), the red dot for the location of the MVCO 12-m underwater node (41.3366° N, 70.5564° W), the green square for the MVCO ASIT at 41.325° N, 70.567° W, and the white marker for the study area. (b) Zoomed-in study area with wave detailed-grid area (dashed lines), flow detailed-grid area (thin solid lines), and the white square at 41.3404° N, 70.459° W for the quadpod of the field experiment (from Pessanha et al. 2023b).

In addition, two bathymetric surveys were conducted in the beginning (16 October 2013) and ending (10 January 2014) of the experiment. Bathymetry was measured using an autonomous water jet drive kayak, Jetyak (Kimball et al., 2015), equipped with a 200 kHz echo sounder and a Post-Processed Kinetic (PPK) GPS system with horizontal and vertical resolution within 2–3 cm and 3–5 cm, respectively. The surveys covered an area of 400m×800m with track lines spaced 30 m from each other. The initial and final bathymetric maps (Figure 6a, b) show the migration of a Y-shaped sand wave, herein just called the sand wave, over the quadpod located in the trough and represented by the white dot. The sand wave migrated towards the northeast, burying the quadpod at the same date as the final bathymetry (Jones & Traykovski 2019). Moreover, the bathymetric surveys show that the sand wave has higher migration speed in the southern portion than the northern portion and indicate counterclockwise rotation of the sand wave.

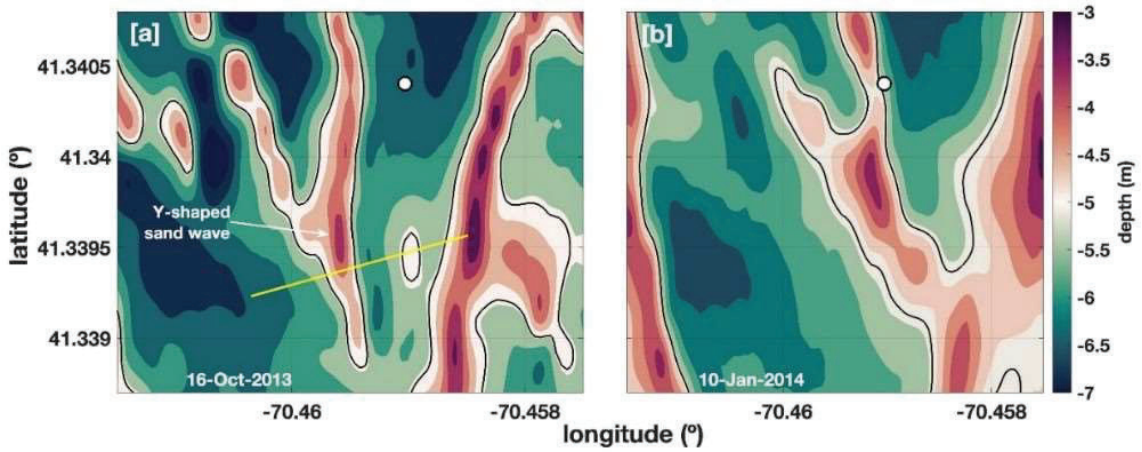

Figure 6. Bathymetric data from the survey performed on (a) 16 October 2013 and (b) 10 January 2014. The white dot marks the location of the quadpod and the black curve represents the 5 m depth. The yellow line illustrates the transect (160 m length) used to calibrate the model (from Pessanha et al. 2023b).

3.3. Dynamics of Underwater Munitions' Mobility and Burial (UnMUMB)

3.3.1. Components of UnMUMB Model

The UnMUMB model has been established to predict munition's mobility and burial on sandy seafloor. The model contains four components: (a) physical parameters of objects such as diameter, length, mass, and rolling moment, (b) dynamics of rolling cylinder around its major axis, (c) empirical sediment scour model, and (d) seabed environmental characteristics such as currents, waves (peak period, significant wave height), sediment density, and medium sediment grain size. Mobility of a seabed object is characterized as the onset fluid velocity at which motion is initiated in relationship to its size and weight (Rennie et al. 2017). The non-dimensional object Shields parameter for percentage burial θ_{opb}, composed from the objects' size and density as well as the local current velocity perpendicular to its main axis (U), was found crucial for the initial mobility of cylindrical object with threshold value of 1 (i.e., $\theta_{opb} > 1$). Burial of a bottom sitting object in sandy sediment is often caused by scour, which is a common burial mechanism and controlled by the fluid velocity in relationship to the surrounding sediment characteristics, such as regional pressure gradients, tidal forcing and the orbital velocity of waves. Other processes beside scour can also bury UXO in non-cohesive sediments. We publish two papers to describe the UnMUMB model development and verification and the User Manuel at the website https://apps.dtic.mil/sti/citations/AD1173688.

Chu, P.C., C.W. Fan, J. Calantoni, and A. Sheremet, 2022: Prediction of mobility and burial of objects on sandy seafloor. *IEEE Journal of Oceanic Engineering*, **47**, No. 1, 2022. https://ieeexplore.ieee.org/stamp/stamp.jsp?arnumber=9552391&tag=1
Chu, P.C., V.S. Pessanha, C.W. Fan, and J. Calantoni, 2021: Coupled Delft3D-object model to predict mobility of munition on sandy seafloor. *Fluids*, **6** (9), 330, https://doi.org/10.3390/fluids6090330.

3.3.2. Dynamics of Munition's Mobility

Let the water velocity (consisting of current and waves) near the seabed ($\mathbf{V}_w$) be in the direction towards the cylindrical munition with an angle, ϕ, perpendicular to main axis of the cylinder, and be decomposed into $\mathbf{V}_w = (U, V)$ with U the perpendicular component, and V the parallel component (Figure 7a) to the main axis of the cylinder. Let (D, L) be the munition's (diameter, length), and B the burial depth. As the munition rolls with angular velocity ω, let the axis of rotation inside the sediment be at depth b ($b < B$) and let ψ be the radial angle of the cylinder from the vertical axis with ψ_B at the top of sediment, and ψ_b at the depth b (Figure 7b). The horizontal velocity of the munition rolling around the point b is given by,

$$u_o = \omega(\frac{D}{2} - b), \tag{1}$$

with the radial component of $u_o \sin\psi$ at any depth inside the sediment. With b as axis of rotation, the sediment above (below) the depth b generates torque to resist (enhance) the rolling with the total torque from the sediment. With the assumption of zero-sum sediment torque for rolling, the ratio $\lambda = b/B$ can be analytically determined by

$$\lambda \equiv b / B = \frac{1 - \cos\left[\tan^{-1}\left(\frac{\psi_B - \sin\psi_B \cos\psi_B}{\sin^2\psi_B}\right)\right]}{1 - \cos\psi_B} \tag{2}$$

The ratio, λ, varies with the burial percentage $p_B = B/D$ mildly from near 0.4445 for $p_B = 0$ and 0.4630. Here, we take λ = 0.453 (Chu et al. 2021, 2022).

The cylindrical munition with large aspect ratio ($L >> D$) is in motion when the object burial percentage Shields parameter θ_{opb} (Friedrichs et al. 2016, Rennie et al. 2017),

$$\theta_{opb} = \frac{C_d \theta_0}{\pi}\left[\frac{1 - p_b/\lambda}{\sqrt{p_b(1-p_b)}}(1 + 2p_\delta - 2p_b) + 2\gamma\right],$$
$$\theta_0 \equiv \left[\frac{U^2}{gD(S_o - 1)}\right], p_\delta = \frac{\delta}{D},\ p_b = \frac{b}{D},\ S_o = \frac{\rho_o}{\rho_w},\ \gamma = \frac{C_l}{C_d} \tag{3}$$

Satisfies the condition,

$$\theta_{opb} > 1 \tag{4}$$

Here, C_d is the drag coefficient; θ_0 is the munition's Shields parameter; p_B is the percentage burial; p_b is the relative depth of the rotation axis in sediment; and S_o is the relative munition's density versus water density.

The corresponding moment of momentum equation including added mass is given by

$$\begin{cases} I_A \dfrac{d\omega}{dt} = T_F - T_B, & \text{if } \; p_B < 0.5, \;\; \theta_{opb} > 1 \\ \omega = 0, & \text{otherwise} \end{cases} \tag{5}$$

where

$$T_F = \frac{1}{2} C_d \rho_w U^2 L \left[\left(D - b/\lambda \right) \left(D/2 + \delta - b \right) + \frac{C_l}{C_d} D \sqrt{b\left(D - b \right)} \right] \left(1 - \frac{u_o}{U} \right)^2 \tag{6}$$

is the forward torque with C_l the lift coefficient and

$$T_B = \frac{\pi}{4} g L D^2 \left(\rho_o - \rho_w \right) \sqrt{b\left(D - b \right)} + \frac{du_o}{dt} \rho_w \Pi (D/2 + B/2 - b) \tag{7}$$

is the backward torque. Let the relative horizontal velocity of the rolling munition be defined by

$$\hat{u}_o = \frac{u_o}{U} \tag{8}$$

which makes $\hat{u}_o$ follow the direction of U. Substitutution of T_B in (7) into (5) leads to

$$\begin{cases} I_A^* \dfrac{d\omega}{dt} = T_F - \Pi(\rho_o - \rho_w)\sqrt{b(D-b)}, & \text{if } \; p_B < 0.5, \;\; \theta_{opb} > 1 \\ \omega = 0, & \text{otherwise} \\ I_A^* = I_A + (D/2 - b)\rho_w \Pi(D/2 + B/2 - b) \end{cases} \tag{9}$$

with

$$I_A = I_o + \rho_o \Pi D^2 / 4 \tag{10}$$

where I_o is the rolling moment about the symmetric axis of the munition; I_A is the rolling moment of munition about the point b (see Figure 7c) using the parallel axis theorem; Π is the volume of the munition.

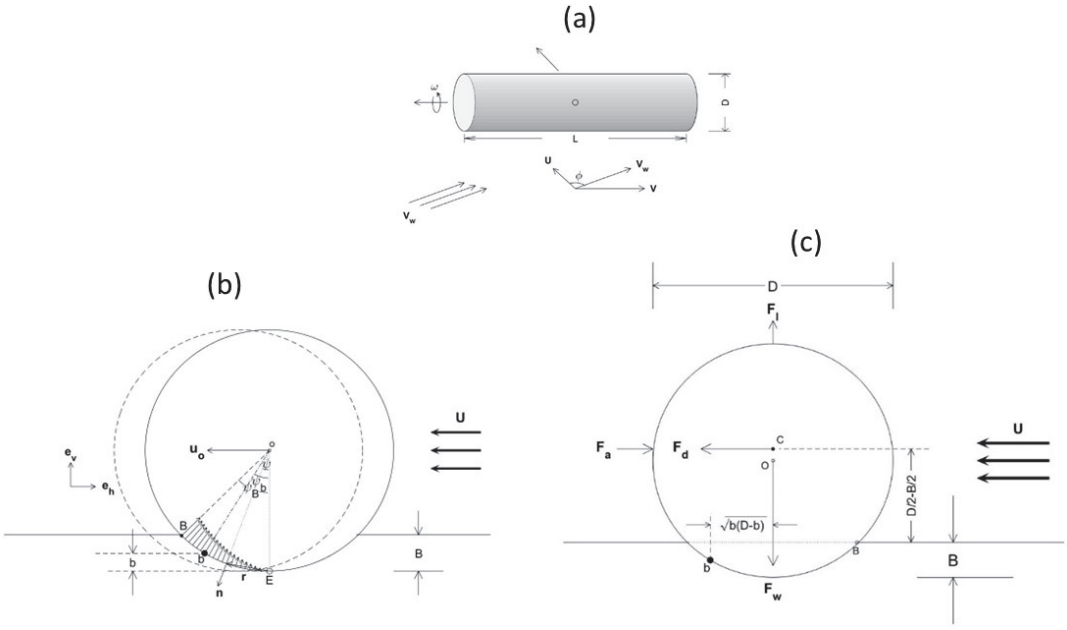

Figure 7. Illustration of munitions' roll dynamics on sandy seafloor: (a) Roll of a cylindrical munition on the seafloor with large aspect ratio forced by the combination of ocean currents and bottom wave orbital velocity with ($\pi/2$-ϕ) the angle between $\mathbf{V}_w$ and the main axis of the cylinder, (b) location of the axis of rotation of the munition in the sediment, b, determined by the assumption of zero-sum torque to the roll, and (c) forces and torques due to drag, lift, buoyancy, and added mass on a partially buried cylinder by combination of ocean currents and bottom wave orbital velocity (U) perpendicular to the major axis of the munition (from Chu et al. 2022).

Substitution of (1), (6) and (8) into (9) leads to the special Riccati equation,

$$\begin{cases} \dfrac{d(1-\hat{u}_o)}{dt} + \alpha(1-\hat{u}_o)^2 = \beta, \ \text{ if } \ p_B < 0.5, \ \ \theta_{opb}(t) > 1 \\ \hat{u}_o = 0, \ \text{ otherwise} \end{cases} \tag{11}$$

where

$$\begin{aligned} \alpha &= \frac{(1-2p_b)}{8I_A^*}\rho_w C_d \,|U|\, D^3 L\left[(1-p_B)(1+p_B-2p_b) + \frac{2C_i}{C_d}\sqrt{p_b(1-p_b)}\right] > 0 \\ \beta &= \frac{(1-2p_b)}{2I_A^*\,|U|} g\rho_w \Pi(S_o - 1) D^2 \sqrt{p_b(1-p_b)} > 0 \end{aligned} \tag{12}$$

The special Riccati Eq (11) has an analytical solution with α_k and β_k as known constants during the integration from t_k to t_{k+1} (k = 0, 1, 2, …, K-1) (Kamke 1977),

$$\hat{u}_o(t)=\begin{cases}1-\dfrac{[1-\hat{u}_o(t_k)]\sqrt{\alpha_k\beta_k}+\beta_k\tanh[\sqrt{\alpha_k\beta_k}(t-t_k)]}{\sqrt{\alpha_k\beta_k}+\alpha_k[1-\hat{u}_o(t_k)]\tanh[\sqrt{\alpha_k\beta_k}(t-t_k)]}, & \text{for } p_B<0.5,\quad \theta_{opb}(t_k)>1\\ 0, & \text{for } p_B\geq 0.5,\quad \theta_{opb}(t_k)\leq 1\\ t_k<t\leq t_{k+1},\quad \alpha_k=\alpha(t_k),\quad \beta_k=\beta(t_k) & \end{cases} \tag{13}$$

Substitution of (13) into (8) leads to the dimensional horizontal velocity of the rolling object, $u_o(t)=U\hat{u}_o(t)$, which should be used for each time interval Δt. The solution (13) depends on (α_k, β_k) which involves three types of parameters: (a) time-independent physical parameters of the object for S_o, Π, L, and D; (b) time-dependent water velocity, $U(t_k)$, from observational data or numerical modeling; (c) time-dependent relative depth of sediment rolling axis [$p_b(t_k)$], and burial percentage [$p_B(t_k)$] determined using a scour burial model. Let l be the displacement of munition,

$$dl/dt=u_o=U\hat{u}(t) \tag{14}$$

Integration of l with respect to time t leads to the munition's displacement. Eqs.(12)-(14) are the key equations for predicting munitions' mobility.

3.3.3. Dynamics of Munition's Scour Burial

Existing studies on scour burial were all concentrated on motionless objects. The ratio between the fluid force (bottom shear stress) and the weight of the sediment particles, i.e., the sediment Shields parameter (θ_{sed}),

$$\theta_{sed}=\frac{F_w U_{br}^2}{g(S_{sed}-1)d_{50}},\quad S_{sed}=\frac{\rho_s}{\rho_w},\quad F_w=\exp\left[5.5\left(\frac{6U_{br}T_P}{\pi d_{50}}\right)^{-0.2}-6.3\right] \tag{15}$$

is crucial for scour burial of motionless object and in turn for prediction of the percentage burial parameter $p_B(t)=B/D$. Here, F_w is the wave friction factor (Nielsen, 1992); U_{br} is the bottom wave orbital velocity; T_P is wave peak- period; ρ_s the sediment grain density; and d_{50} the medium sand

grain size. Another frequently used dimensionless parameter to describe scouring and ripple burial of a cylinder of diameter D is the Keulegan-Carpenter (KC) number,

$$KC=\frac{T_P U_{br}}{D} \tag{16}$$

which represents the ratio of the excursion of the wave orbital velocities to the diameter of the cylindrical munition. It can therefore be applied to parameterizing the scour properties around

cylinders based on the size of the vortices induced by the orbital velocities. The threshold for the initiation of scouring due to vortices at the ends of a cylinder is $KC^{*} = 2$, and the threshold for the periodic burial by migrating ripples is $KC^{**} = 14$ (Voropayev et al. 2003).

The bottom wave orbital velocity U_{br} represents interactions between surface waves and the seabed. For small-amplitude, monochromatic waves, linear wave theory predicts that the horizontal component of orbital velocity reaches a maximum velocity since the vertical component approaches zero at the ocean bottom, which leads to

$$U_{br} = \frac{2\pi}{T \sinh(kh)} A \tag{17}$$

where T is the wave period; k is the wave number; and A is the wave amplitude. However, wind-generated waves are not monochromatic. Instead, a spectrum of wave frequencies and heights are present. A spectrum of wave-induced orbital velocity at the bottom boundary can be calculated from a surface gravity wave spectrum $S\eta$ by applying (17) to each frequency band i of the wave spectrum (e.g., Soulsby 1987),

$$U_{br}^2 = 2\sum_i \left[\frac{2\pi}{T_i \sinh(k_i h)} \right]^2 S_\eta(f_i) \Delta f_i \tag{18}$$

where $f_i = 1/T_i$, is the wave frequency. Direct measurements of wave spectra from nearby surface-wave buoys are ideal for determining bottom orbital velocity time series for a site of interest. When the measurements of surface gravity wave spectra are not available, a general form of wind-generated wave spectra can be used (Wiberg & Sherwood 2008)

$$S_\eta(f) = \frac{\xi_1 H_S^2 f_p^4}{16 f^5} \left(\frac{f}{f_p} \right)^{\xi_4} \exp\left[-\xi_2 \left(\frac{f}{f_p} \right)^{-4} \right] \xi_3^{\exp\left[-\left(f - f_p\right)^2 / (2\xi_5^2 f_p^2) \right]} \tag{19}$$

where $f_p = 1/T_p$, is the wave peak frequency; H_S is the significant wave height; and (ξ_1, ξ_2, ξ_3, ξ_4, ξ_5) are spectral parameters. A MATLAB function was created to calculate bottom orbital velocity using the parametric spectrum (19) with the water depth (h), significant wave height (H_S), and peak period (T_p) as input and the bottom orbital velocity (U_{br}) as output (see Appendix *D* in Whitehouse, 1998). In this project, we use the JONSWAP spectrum (Hasselmann et al. 1973).

As pointed in Rennie et al. (2017), the equilibrium percentage burial $p_{B,eq}$ for motionless cylinders induced by scour tends to increase as θ_{sed} increases. An empirical formula has been established,

$$p_{B,eq} = a_1 \theta_{sed}^{a_2} - a_3 \tag{20}$$

with different choices of the coefficients (a_1, a_2, a_3) determined experimentally for cylinders subject to steady currents: $a_1 = 11$, $a_2 = 0.5$, $a_3 = 1.73$ (Whitehouse 1998), $a_1 = 0.7$, $a_2 = a_3 = 0$ (Sumer et al., 2001), $a_1 = 2$, $a_2 = 0.8$, $a_3 = 0$ (Demir and Garcia, 2007), and for cylinders under waves (depending on wave period): $a_1 = 1.6$, $a_2 = 0.85$, $a_3 = 0$ for T_p longer than 4 s (Cataño- Lopera, 2007). For motionless cylinders before scour burial reaches an equilibrium the percentage burial follows an exponential relationship (Whitehouse 1998),

$$p_B(t_k) = p_{B,eq}\left[1 - \exp\left(-\frac{t_k}{T*}\right)\right] \tag{21}$$

where the e-folding time scale T* is given by

$$T* = \frac{M\theta_{sed}^{N} D^2}{\left[g(S_{sed} - 1)d_{50}^3\right]^{0.5}}, \quad N = 1.5, \quad M = 0.11 \tag{22}$$

The model for munition ‘s scour burial contains Eqs (15), (18)-(22). Thus, the UnMUMB model consists of Eqs (12)-(15), (18)-(22).

3.4. Delft3D Model

An open-source software, Delft3D, has been developed to predict currents, waves, sediment transport, and morphology in estuarine, fluvial, and littoral environments (Deltares 2019a, b; Booij et al. 1999). The Delft3D version 4.04.01 was implemented to the northern Gulf of Mexico near Panama City, Florida (i.e., TREX13 field site, lower energetic environment) and the Wasque Shoals (strong tidal currents and intermittent energetic wave events), about 1 km from the southeastern corner of Martha's Vineyard, Massachusetts with three major modules: Flow (tides and circulations), Wave (wave propagations, Morphology (sediment transport and morphological evolution).

The Delft Dash Board (DDB) was used to create the grids and the tide forcing boundary conditions for the coupled wave and 2D flow model, including sediment transport and bottom change. Four nested grids compose the wave model, while two nested grids constitute the flow model. Wave boundary conditions were set up including output of Wavewatch III and measurements from NOAA Buoy. Moreover, wind data and bathymetric data from ECMWF and NOAA/NGDC, respectively, were incorporated as input data to the coupled model. The parameter settings for the flow, wave, and morphology modules are also provided. Most information in this section can be found in the three papers:

Pessanha, V.S., P.C. Chu, and M.K. Gough, 2022: Sediment accretion in a lower-energetic location during two consecutive cold fronts. *Journal of Operational Oceanography*, http://doi.org/10.1080/1755876X.2022.2100145
Pessanha, V.S., P.C. Chu, M.K., Gough, and M.M. Orescanin, 2023: Coupled model to predict wave-induced liquefaction and morphological changes. *Journal of Sea Research*, **192**, https://www.sciencedirect.com/science/article/pii/S1385110123000187?via%3Dihub.
Pessanha, V.S., P.C. Chu, M.K., Gough, and M.M. Orescanin, 2023: Sand wave migration near the southeastern corner of Martha's Vineyard, Massachusetts, USA. *International Journal of Sediment Research*, **38**, https://doi.org/10.1016/j.ijsrc.2023.04.006.

3.5. Coupled Delft3D-UnMUMB Model

Delft3D output provides the environmental parameters around the munition, which are required by the UnMUMB model for predicting the munition's burial and mobility. Under the sponsorship of SERDP, experimental (Calantoni et al, 2014; Traykovski and Austin 2017) and analytical (Friedrichs et al., 2016; Rennie et al. 2017) studies focus on the determination of the conditions that determine the onset of a specific and important motion, i.e., roll of munition around its main axis, both on a hard surface and on a sand bed in the presence of concurrent scour burial. In this study, a coupled Delft3D-object model has been developed to predict hydrodynamic and morphological processes as well as munitions' burial and mobility on the sandy sea floor. The Delft3D model output was taken as the forcing term for the object model (Figure 8).

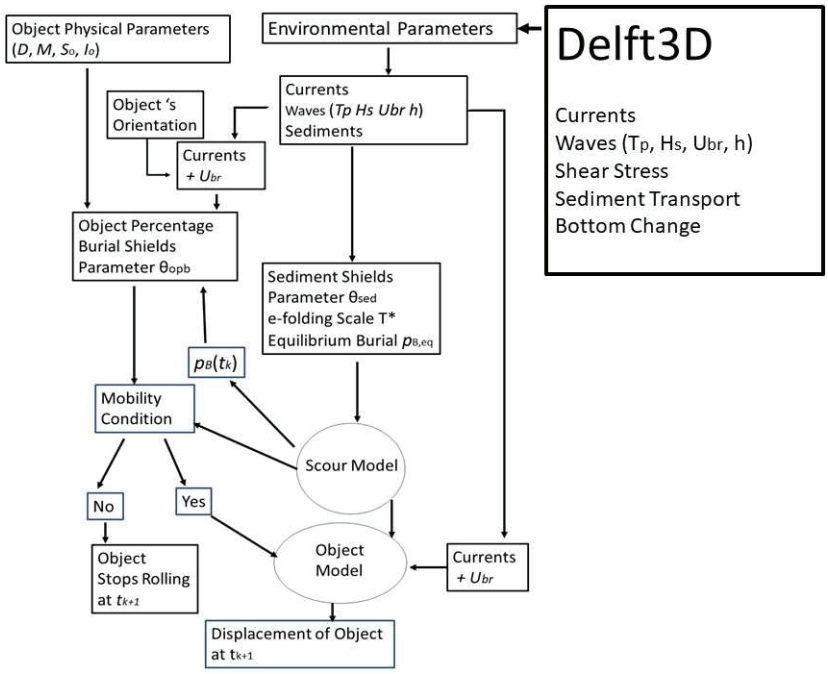

Figure 8. Flow chart of the coupled Dlft3D-UnMUMB model to predict munitions' mobility and burial (from Chu et al. 2021).

The coupled system consists of two major components: Delft3D and object model. The object model has five parts: (a) cylindrical object model with the burial percentage Shields parameter (θ_{opb}), (b) sediment scour model with sediment Shields parameter (θ_{sed}), (c) object's physical parameters such as diameter (D), object's relative density versus water density (S_o), mass (M),

rolling moment about its symmetric axis (I_o), (d) environmental variables such as near seabed ocean currents, bottom wave orbital velocity (U_{br}) water depth (h), wave peak period (T_P), significant wave height (H_S), sediment characteristics, and (e) model output such as the burial percentage p_B, and the object's displacement. We provide the detailed information about the coupled UnMUMB-Delft3D modeling in the following paper:

Chu, P.C., V.S. Pessanha, C.W. Fan, and J. Calantoni, 2021: Coupled Delft3D-object model to predict mobility of munition on sandy seafloor. *Fluids*, **6** (9), 330, https://doi.org/10.3390/fluids6090330.

3.6. Assessment of Model Performance

Let X be the variable of interest (e.g., significant wave height, water level, current velocity, seafloor pressure, …); X_{mod} be the model output; X_{obs} be the observation; N the number of observations; and $\langle X \rangle$ be the temporal mean. We use the root mean square error (*RMSE*),

$$RMSE = \sqrt{\frac{1}{N}\sum (X_{\text{mod}} - X_{obs})^2} \tag{23}$$

and the skill score (SS)

$$SS = 1 - \frac{\left(\sum \left| X_{\text{mod}} - X_{obs} \right|^2\right)}{\left[\sum \left(\left| X_{\text{mod}} - \langle X_{obs} \rangle \right| + \left| X_{obs} - \langle X_{obs} \rangle \right| \right)^2\right]} \tag{24}$$

to assess the model performance and the model prediction skill (Willmott 1981). As discussed by Krause etal. (2005), perfect agreement between model output and observations if SS = 1, and totally disagreement if SS = 0.

4. Results and Discussions

4.1. Deep Scour Burial

We have made two contributions. First, we developed a new method on the base of angle of repose of sediment to identify munition's deep scour burial using the sonar imagery. Second, we proposed a new power law to combine shields parameter (θ) and KC number to predict the deep scour burial. The results were presented in the following paper.

Gough, M.K., P.C. Chu, Pessanha, V.S., and J. Calantoni, 2022: Deep burial of a tapered cylinder by an energetic wave event. *IEEE Journal of Oceanic Engineering*, **47**, IEEE Xplore.ieee.org/stamp/stamp.jsp?tp=&arnumber=9976217

4.1.1. New Formula to Identify Scour Ridge Heigh Using Sonar Imagery

Surrogate munitions were deployed as representations of real munitions with similar shapes and densities within the field-of-view of the rotary sonar (Calantoni et al., 2014). While many surrogates were deployed at the 7.5 m quadpod, three were most clearly visible in the sonar imagery at the time of the wave event and are labeled D6, D3, and C6 in Figure 9a. Analysis is focused on the burial of D6 which has an overall length of 58.4 cm, a maximum diameter of 15.5 cm, and a bulk density of 4456 kg/m^3 (Figure 9b)

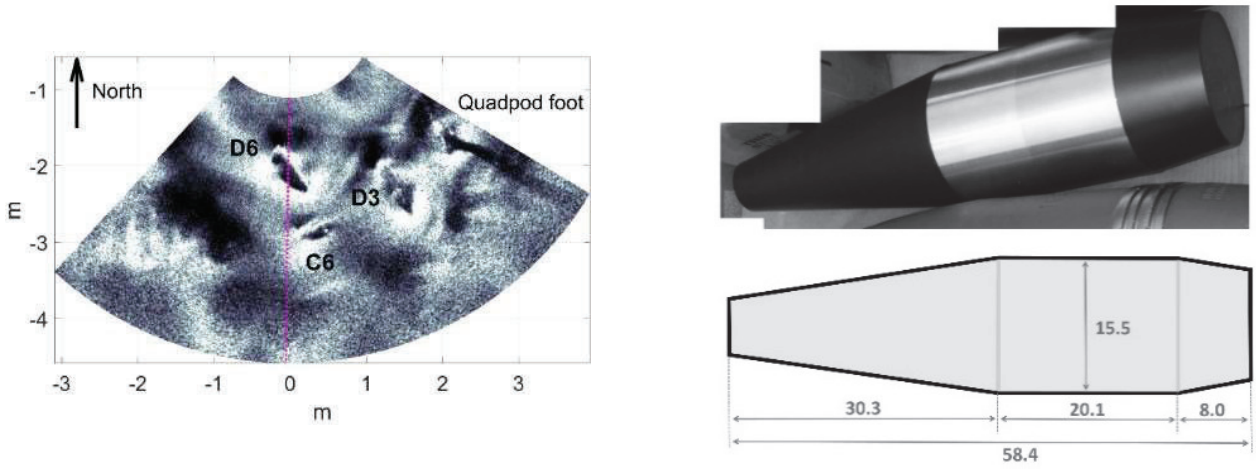

Figure 9. (a) A 4-hr averaged sonar image centered on 5 May hour 22 in TREX13. Surrogate munitions are labeled D6, D3 and C6. The magenta dashed line indicates the transect for determining shadow and scour ridge positions. (b) Surrogate D6 tapered cylinder (top) photograph and (bottom) side view diagram. Dimensions are in mm. Not shown is a stainless steel rod that was used to connect the tapered sections (Delrin plastic) to the center cylindrical section (stainless steel) (after Gough et al. 2022).

For each sonar image the range distances r_A, r_B, and r_C along a transect are collected where r_A denotes the top of munition, r_B denotes the edge of the shadow cast by munition on the scour ridge, and r_C denotes the crest of the scour ridge. The range distance to sonar beam intersection at the top of D6, denoted by r_A, remained constant. The chosen range transect crosses the wide part of the munition which is known to have diameter D = 15.5 cm.

We identify the seabed near-field scour ridge height (S) of an object with diameter (D) from the deployed rotary scanning sonar imagery. On the base of angle of repose, we derived the following formulae to compute h (see Figure 10)

$$h = (r_B - r_A)\tan\alpha + \frac{(0.5D)^2}{\sqrt{a^2m^2 + (0.5D)^2}} \tag{25}$$

where r_A and r_B are known, and the angle from horizontal of sonar beam α as a function of range known, the height at r_B relative to the bottom of munition can be accurately determined as where m is the slope of α, and a is the major axis of the ellipse created by the sonar beam intersection with munition. The scour ridge height relative to the bottom of munition is then estimated as

$$S_{obs} = 0.5D - (r_C - r_B)\tan\phi + h \tag{26}$$

where ϕ is the angle of repose of the scour pit. In Eqs. (25) and (26), the only unknown parameter is ϕ. The height of the munition above the seabed is then estimated S_{obs}/D, referred to as the relative scour depth $[S/D]_{obs}$. If ϕ is given, $[S_{obs}/D]$ can be totally determined was determined from the sonar image. For well sorted (uniform) sand, ϕ has been estimated to be between 20° and 40° (Li and Komar, 1986), and is typically assumed to be 32° (Demir and García, 2007). Since sand samples obtained at the quadpod were reported to be well-sorted (Calantoni et al., 2014), and small backscatter intensity at the scour pit north of D6, along with an estimated beam angle of 30° over the scour pit, ϕ is likely slightly greater than the estimated sonar beam angle over the scour pit which supports the assumption that ϕ is nearly 32°.

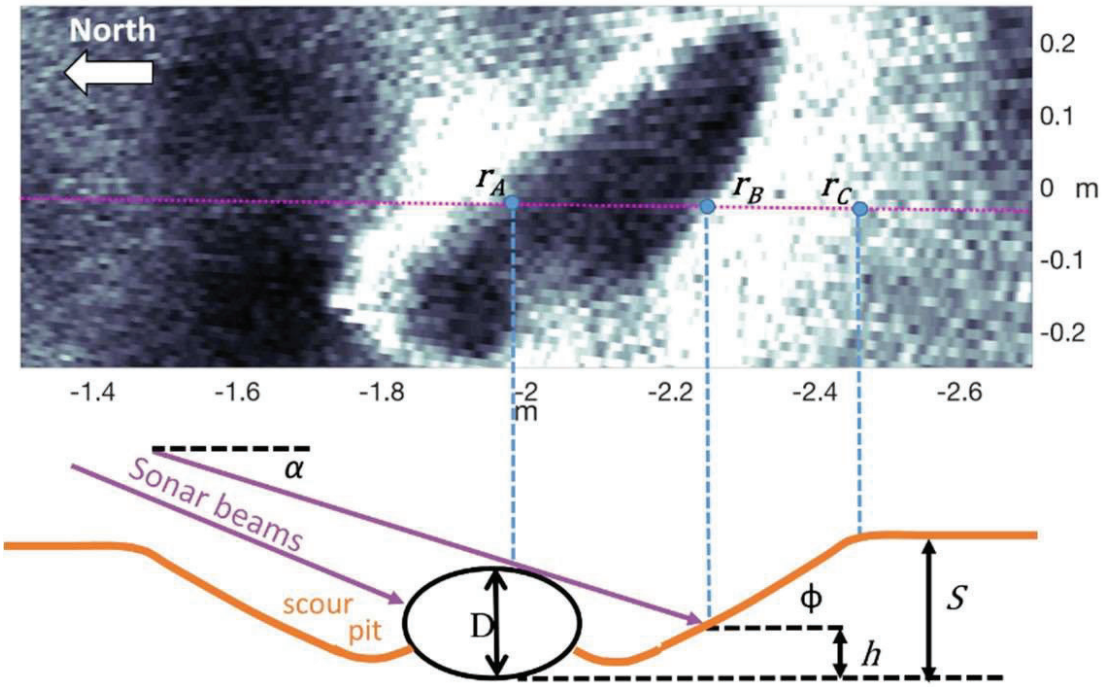

Figure 10. (top) Sonar image at hour 22 on 5 May of the D6 surrogate in TRAX13. The image has been rotated so that North is pointed to the left. Points r_A, r_B, and r_C indicate the positions of the leading edge of D6, the shadow on the scour slope, and the scour ridge crest respectively. The dashed magenta line is the same as in Figure 9a. (bottom) Notional cross-sectional representation of the transect of the above sonar image identified by the dashed magenta line (from Gough et al. 2022).

The log-time series of TREX13 near the shallow quadpod (location shown in Figure 2a) includes sonar imageries, observed u (east-west) and v (north-south) components of horizontal velocities by a downward looking PC-ADP from the seabed to 80 cm above the bed with a vertical resolution of 5 cm and a temporal resolution of 2 Hz, and observed waves and currents by an upward looking AWAC with AST in 30-minute bursts with one-minute averaged horizontal velocities at 50 cm bins to the sea surface for 10 minutes and distance to the sea surface with a temporal resolution of 4 Hz for 20 minutes. The orange lines indicate the sand bottom. D and S indicate the diameter of D6 and the scour ridge height, respectively. α and ϕ indicate the sonar beam angle from horizontal and the angle of repose, respectively.

4.1.2. New Power Laws with Shields Parameter and KC Number

The time series of $[S/D]_{\text{obs}}^{\text{TREX13}}$ is obtained from the sonar imagery. The time series of the shields parameter θ and KC number are calculated from the PC-ADP/AWAC data. om log-linear regression performed on $\left[S/D\right]_{\text{Obs}}^{\text{TREX13}}$ as a function of θ, KC, and (θ*KC) the predicted power law relationships are determined as

$$\left[S/D\right]_{\text{regress}}^{\text{TREX13}} = \begin{cases} 1.42\theta^{0.42}, & R^2 = 0.77 \\ 0.11KC^{0.72}, & R^2 = 0.69 \\ 0.55(\theta \times KC)^{0.27}, & R^2 = 0.75 \end{cases} \quad (27)$$

which are represented by the black line in Figure 11 where the data points for $\left[S/D\right]_{obs}^{\text{TREX13}}$ are color coded by time, and for previous studies are represented by the various grey lines. There is good confidence in the regression analysis with sufficiently high correlation coefficients.

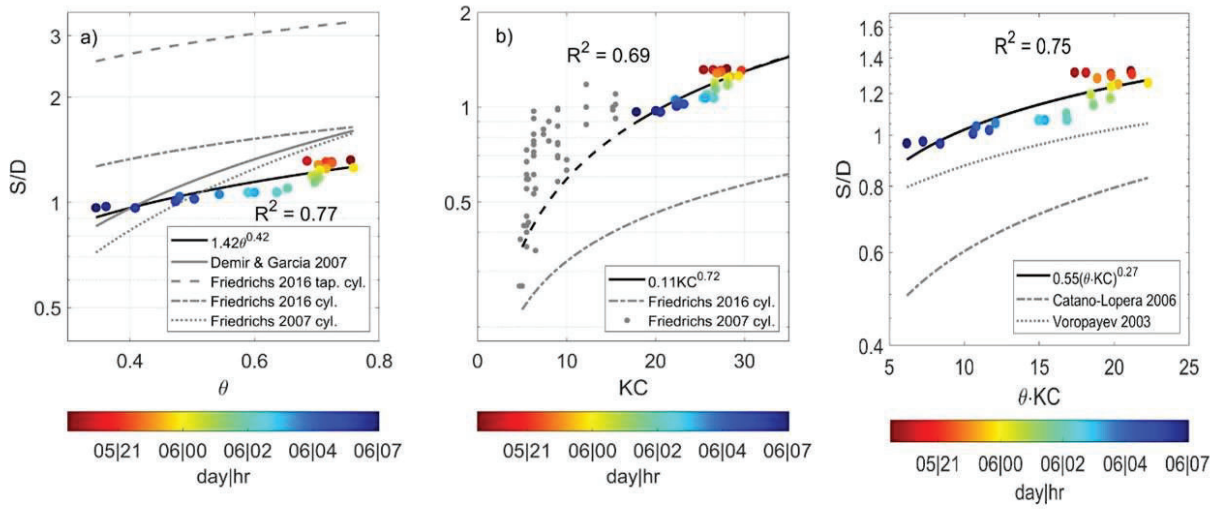

Figure 11. Representation of the three power laws with R^2 value included: (a) scatter plot of $[S/D]_{obs}$ (color coded dots by time) and the power law relationship representing $S(\theta)_{eq}^{TREX13}$ (black line), (b) scatter plot of $[S/D]_{obs}$ and the power law relationship representing $S(KC)_{eq}^{TREX13}$ (black line), and (c) scatter plot $[S/D]_{obs}$ (color dots) and power law relationship of $S(\theta \cdot KC)_{eq}^{TREX13}$ (black line). Power law relationships from previous studies are indicated by the various grey lines. The dashed black line is an extension of $S(KC)_{eq}^{TREX13}$. The grey dots are from Friedrichs (2007), and the grey dashed line indicates the historical synthesis of S/D observations reported by Friedrichs (2016). The y-axes are log-scaled. The grey dashed lines indicate $S(\theta \cdot KC)_{eq}$ relationships reported by Catano-Lopera (2006) and Voropayev (2003). The y-axis is log-scaled (from Gough et al. 2022).

Different power laws shown in Figure 11 are caused by the laboratory and field experiments. Laboratory experiments may have difficulty replicating scour-induced burial in random wave environments, and there may be other processes contributing to scouring that are not adequately reproduced in laboratory experiments. Possible additional differences in the physical environment between field and laboratory studies are numerous and include limitations in the way laboratory studies typically represent infra-gravity waves, longshore currents, directional wave spreading, and site-specific sedimentology. Owing to the numerous factors that contribute to scouring it is not possible to pinpoint the exact cause for the observed discrepancies; however, it is worth further discussion.

4.2. Coupled Delft3D and Wave-Induced Liquefaction Modeling

We coupled Delft3D and wave-induced liquefaction model to predict morphological changes and seafloor instability. The Delft3D model is employed to predict water level, currents, waves, and seafloor evolution and provide the forcing term to the wave-induced liquefaction model. The model is validated using observations during TREX13 from instrumentation attached to two quadpods moored at the 7.5 and 20 m bathymetric contours off the coast of Panama City, Florida (Figure 12). The field data include seafloor elevation relative to the instrumentation at the shallow quadpod, obtained from pencil beam sonar observations, and the maximum backscatter from the pulse coherent acoustic Doppler profiler. Observations determined that the seafloor elevated by 0.05 m during the first wave event and by a previously observed 0.1–0.15 m during the second wave event. By comparing the water level observed by a nearby NOAA tide station, it is determined that the 0.05 m seafloor elevation increase during the first wave event is attributed to sediment accretion, whereas the 0.1–0.15 m elevation increase during the second wave event is attributed to settling of the shallow quadpod into the sandy seafloor. The coupled model output is used to build maps of liquefaction degree and estimated failure depth. Results indicate liquefaction occurred in areas with depth/wavelength ratios smaller than 0.25, which is consistent with a previously observed sinking of the shallow quadpod sank during the second wave event. Model output also indicates a seafloor elevation of up to 0.05 m, suggesting that both liquefaction and sedimentation occurred near the shallow quadpod. Detailed information can be found in the following paper:

Pessanha, V.S., P.C. Chu, M.K., Gough, and M.M. Orescanin, 2023a: Coupled model to predict wave-induced liquefaction and morphological changes. *Journal of Sea Research*, **192**, https://www.sciencedirect.com/science/article/pii/S1385110123000187?via%3Dihub

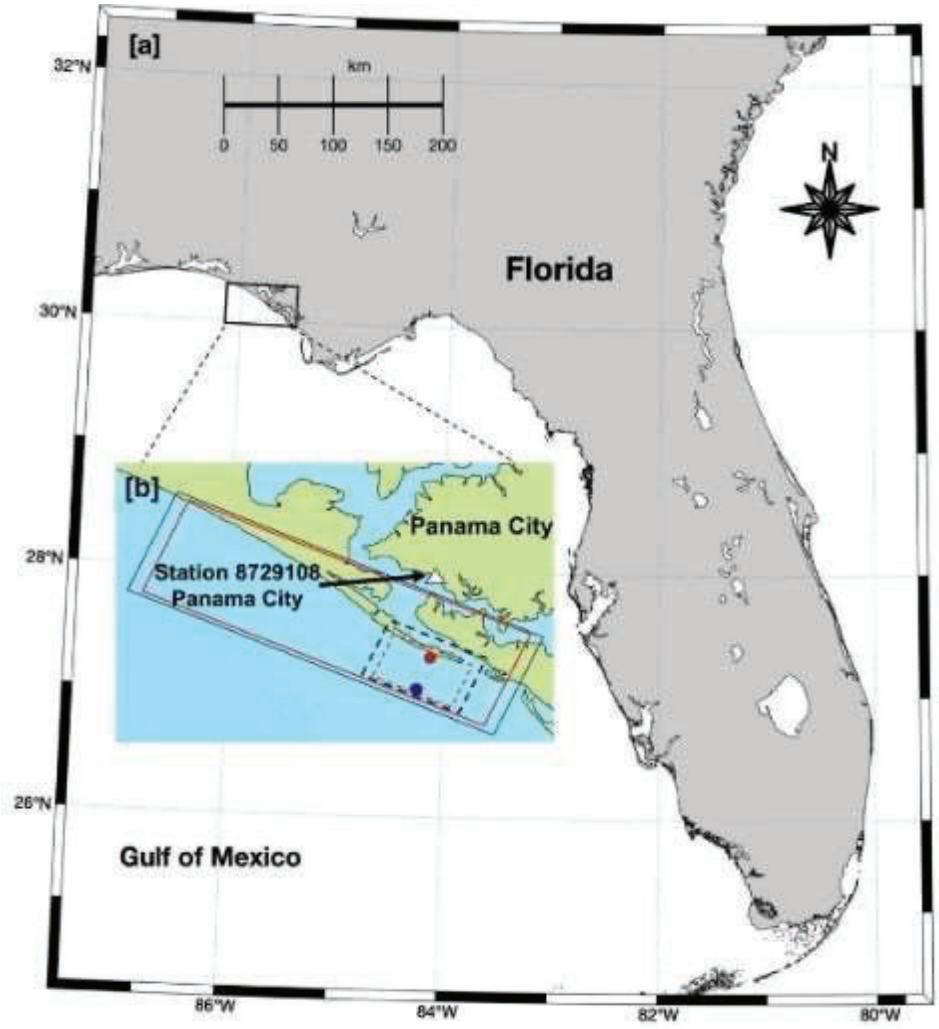

Figure 12. Northern Gulf of Mexico. (a) Location of the coast of Panama City indicated by the black rectangle. (b) NOAA station 8729108 (white triangle) at 30.152° N, 85.7° W, model domain area with enclosures for wave outer (black line), flow outer (red line), wave inner (dashed black line), and flow inner (dashed red line) computational grids. The red dot represents the shallow quadpod location (30.08°N, 85.673°W), and the blue dot denotes the deep quadpod location (30.05°N, 85.689°W) (from Pessanha et al. 2023a).

4.2.1. Wave-Induced Liquefaction Model

The occurrence of wave-induced liquefaction is estimated using the method introduced by Klammler et al. (2020), in which the wave-induced pore pressure over the seafloor surface, P_p, is represented by

$$P_p(x,t) = \sum_{m=1}^{M} a_m \cos(k_m x - \omega_m t + \varepsilon_m) \tag{28}$$

where t is time; x is the horizontal location in the direction of wave propagation; (a_m, k_m, ω_m, ε_m) are (amplitude, wavenumber, angular frequency, phase angle) of the m-th mode; and M is the total number of modes. The dispersion relation of the surface gravity waves is given by

$$\omega_m^2 = g k_m \tanh(d k_m), \tag{29}$$

where g is the gravity acceleration and d is mean water depth. The wave-induced pore pressures (p_p), horizontal (σ'_x) and vertical (σ'_z) effective stresses, and shear stress (τ_{xz}) are determined analytically by (Hsu & Jeng, 1994; Klammler et al. 2020)

$$\begin{bmatrix} p_p \\ \sigma'_x \\ \sigma'_z \\ \tau_{xz} \end{bmatrix} = \mathrm{Re}\left\{ \sum_{m=1}^{M} a_m \begin{bmatrix} P \\ -S_x \\ S_z \\ iT \end{bmatrix} \exp\left[i\left(k_m x - \omega_m t + \varepsilon_m \right) \right] \right\}, \tag{30}$$

where Re{ } is the real part of a complex quantity; i denotes the imaginary unit; z is the vertical coordinate; P, S_x, S_z, and T are complex parameters depending on complex constants and seafloor properties such as porosity (n), horizontal (K_x) and vertical (K_z) conductivities, degree of saturation (S_r), shear modulus (G), Poisson ratio (μ), density of sea water (ρ_w), elastic modulus of sea water (K_w), and mean water depth (d). The computation of the complex parameters involves approximately 100 expressions described by Jeng (2018). In addition, Klammler et al. (2020) went into further detail regarding how the complex parameters and constants are computed. The seafloor and sea water properties used in the computation of the analytical solution are based on Klammler et al. (2020) and listed in Table 2.

Table 2. Seafloor and sea water properties applied to the wave-induced liquefaction model.

n [-]	K_x [m/s]	K_z [m/s]	S_r [-]	G [N/m^2]	μ [-]	ρ_w [kg/m^3]	h [m]	K_w [N/m^2]
0.3	10^{-4}	10^{-4}	0.98	10^7	0.3	1025	100	2×10^9

The liquefaction degree (L) defined by

$$L = \begin{cases} \lim\limits_{z\to 0^-} \left[\left(-\gamma_w \sigma'_z \right) / \left(\gamma_s - \gamma_w \right) z \right] & \text{if } \sigma'_z > 0, \\ 0 & \text{if } \sigma'_z \le 0, \end{cases} \tag{31}$$

is used to represent sediment failure criterion (Jia et al., 2014). Here γ_w and γ_s are the weights of seawater and saturated sediment. As the liquefaction potential is greatest just beneath the seafloor surface, the limit in Equation (31) is evaluated for z tending to 0^-. Negative values of σ'_z cause a compressive effect on the sediment and act to stabilize it ($L = 0$). Positive σ'_z values, on the other hand, enhance sediment buoyancy and raise the risk of seabed instability ($L > 0$). Values of $L \geq 1$ may indicate an extreme circumstance where the sediment grains float, resulting in a limited and transient episode of wave-induced liquefaction.

4.2.2. Seafloor Evolution Predicted by Delft3D

The model predicts seafloor changes on 7 May 0600 (Figure 13) after the second wave event with approximately 0.05 m of sediment accretion around the shallow quadpod location. In addition, the model predicts erosion (blue areas) near de coast extending to approximately 200 m offshore and sediment accretion (red and yellow areas) from 200 m to approximately 1 km from the coast. Some sediment accretion areas also appear where erosion is predominant (first 200 m from the coast).

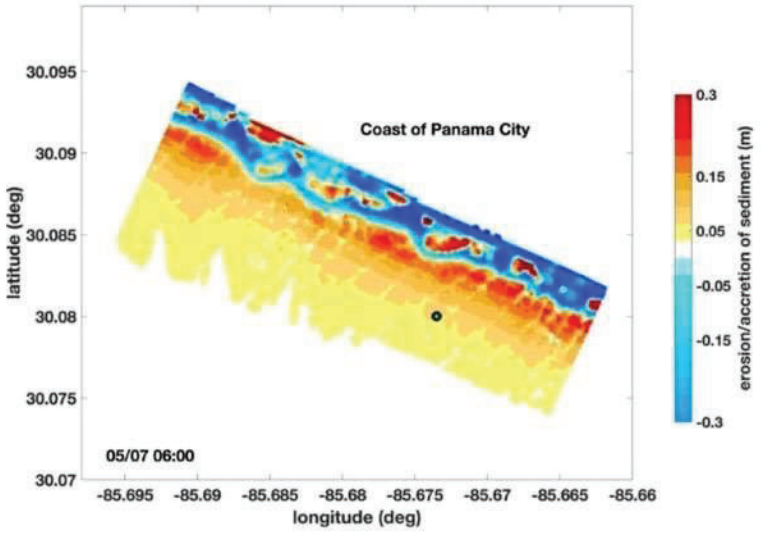

Figure 13. Model output for erosion (blue areas) and accretion of sediment (red and yellow areas) on 7 May 0600. The shallow quadpod location is represented by the green dot (from Pessanha et al. 2023a).

The model result at the shallow quadpod location in TREX13 (Figure 2a) shows that the bedload sediment transport is nearly zero during the entire period. The sediment is transported primarily in suspension (Figure 14a). The peaks of suspended load transport are associated with peaks of H_s and strong backscatter observed in the water column (Figure 14b). The backscatter of the water column from the seafloor up to 0.6 m and the observed seafloor elevation from the PC-ADP maximum backscatter (black line) and pencil beam sonar (white dot). An increase in suspended sediment over the water column is noted (greenish/yellowish colors) during the first wave event, between 4–5 May, and an observed seafloor elevation by up to 0.05 m from the PC-ADP maximum backscatter and 0.04 m from the pencil beam sonar. Moreover, the backscatter of suspended

sediment is even stronger (yellowish/reddish colors) during the second wave event, between 5–6 May, with an additional seafloor elevation by up to 0.15 m from the PC-ADP maximum backscatter and by 0.1 m from the pencil beam sonar. On 6 May, the seafloor elevation from the PC-ADP maximum backscatter decreased 0.05 m and presented a variation by 0.05 m again between 6–8 May. Observations from the pencil beam sonar presented in the same period but with a smaller amplitude (between 0.02–0.03 m), which may be attributed to sand ripples migration. This is consistent with Penko et al. (2017) showing the formation of ripples at the shallow quadpod location during that time.

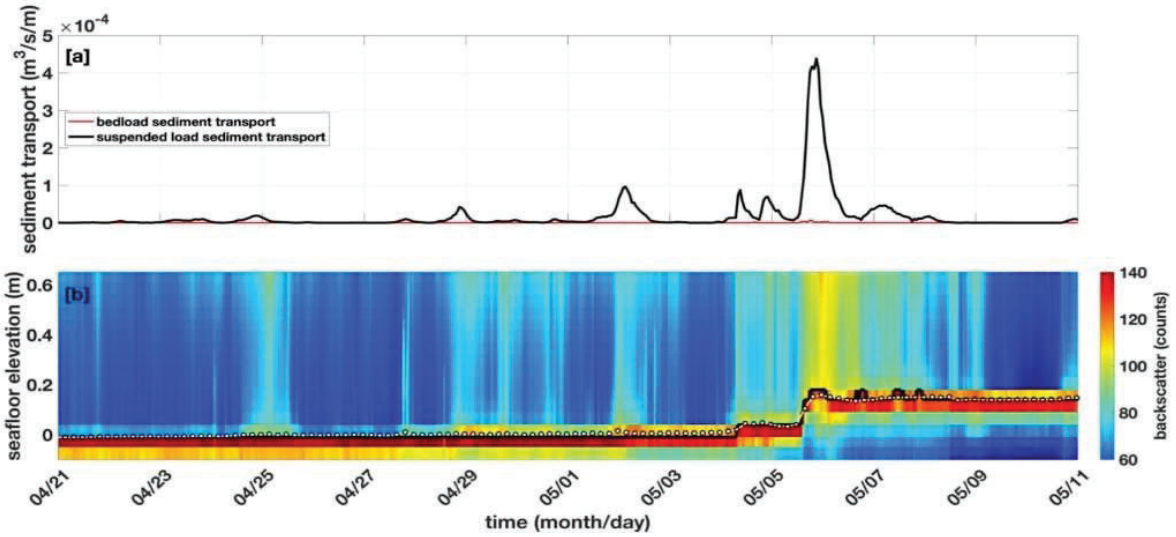

Figure 14. (a) Suspended load (blue line) and bedload sediment transport (red line) from the model output. (b) Backscatter of the water column from the seafloor up to 0.6 m from the PC-ADP. Seafloor elevation is determined from the PC-ADP maximum backscatter (black line) and the pencil beam sonar (white dots). Both model output and observations refer to the shallow quadpod location (from Pessanha et al. 2023a).

4.2.3. Factors for Liquefaction

Figure 15 depicts the dependence of *L* on water depth (Figure 15a), dissipation of wave energy on water depth (Figure 15b), as well as wave steepness (*Hs*/wavelength) on relative water depth (water depth/wavelength) (Figure 15c) with respect to color-scaled failure depth using the model output during the second wave event. Figure 15a indicates failure depth occurrence in areas shallower than 10 m, which can be identified by the points above the threshold line of L=1, and the peak of L occurring around 4 m depth. However, L and failure depth decrease in depths shallower than 4 m. From 4 m depth, the dissipation of wave energy increases at a greater rate towards the shore, as shown in Figure 15b, in which failure depths decrease when the dissipation of wave energy is greater than 40 N/ms. Furthermore, relative water depth is a prominent feature, with failure depth decreasing as relative water depth increases, and no liquefaction is predicted for relative water depths greater than 0.25. (Figure 15c). Despite the small wave steepness variability shown in Figure 15c, the largest failure depths are predicted for wave steepness between 0.045 and 0.06.

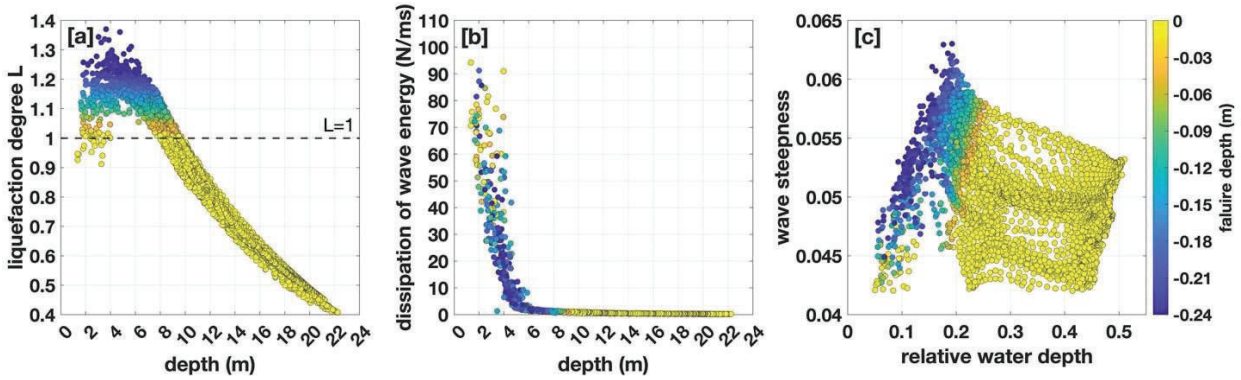

Figure 15. Scatter plot of (a) liquefaction degree (L) and depth, (b) dissipation of wave energy and depth, (c) wave steepness and relative water depth. Colors denote the failure depth as scale on the right panel (c). The black dashed line on panel (a) represents L = 1. Scatter plots consider model output during the second wave event (from Pessanha et al. 2023a).

Additionally, the model was run for 12 different conditions of H_s and T_p by imposing wave boundary conditions distinct from those observed in the deep quadpod used in the main simulation. In these simulations, combinations of H_s (1, 2, and 3 m) and T_p (7, 8, 9, and 10 sec) were considered. The wave conditions (H_s, T_p, θ_{dir}) were kept constant in time throughout the simulations with θ_{dir} *approximately* perpendicular to the coast (220º), during the second wave event. Moreover, the duration of simulation was limited to 6 h to reduce the computational cost, starting on 5 May 1600, before the second wave event. Except for the change in wave boundary conditions and duration, all other parameters were remained the same, as described in subsection
2.2. For simulations with H_s=1 m, L was less than 1 over the area of interest, and no liquefaction was predicted. In contrast, liquefaction was identified from model simulations with H_s=2 m, 3 m and T_p=7, 8, 9, 10 s (Figure 16). For both H_s=2 m and H_s=3 m, T_p=7 s presented larger L than T_p=10 s, possibly owing to the rapid dynamics of pressure fluctuations affecting the excess pore pressure. In addition, liquefaction ($L \geq 1$) was predicted for relative water depth ranging from 0.05 to 0.42 for H_s=3m (Figure 16a) and from 0.05 to 0.37 for H_s=*2* m (Figure 16c). Regarding the wave steepness, liquefaction was indicated from 0.03 to 0.09 for H_s=3m (Figure 16b) and from 0.025 to 0.075 for H_s=*2* m (Figure 16d). Larger waves (H_s=3m) cover a broader range of relative water depth and wave steepness, with higher values of relative water depth and wave steepness associated with shorter T_p (7 s).

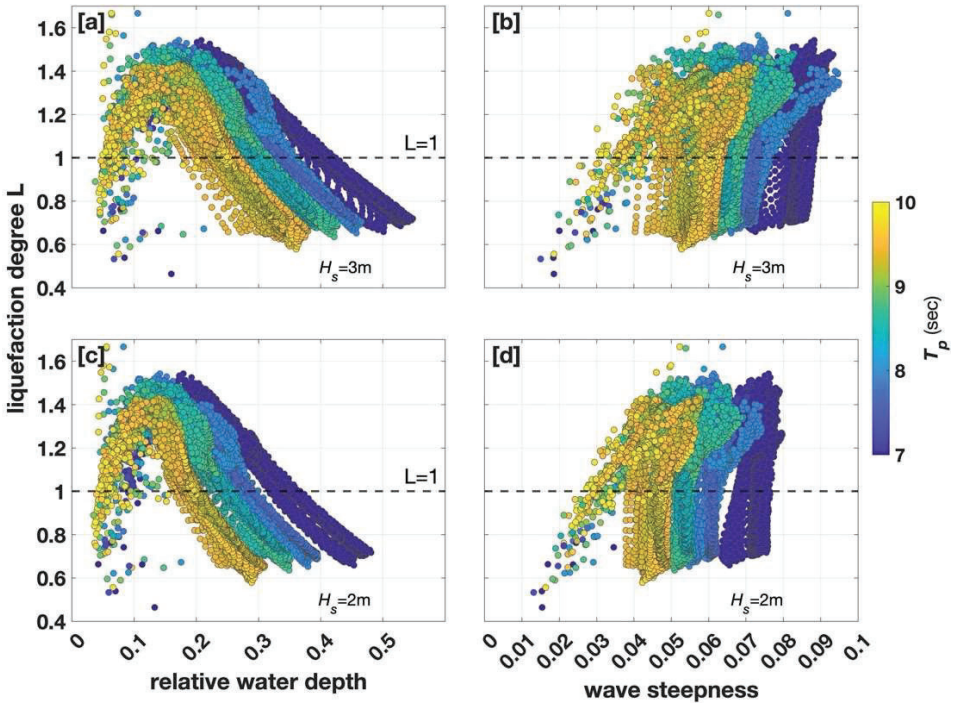

Figure 16. Dependence of liquefaction degree (L) on (a) relative water depth for H_s=3 m, (b) wave steepness for H_s=3 m, (c) relative water depth for H_s=2 m, and (d) wave steepness for H_s=2 m from model output. Color scales denote the wave peak period (T_p). The black dashed line represents L=1 (from Pessanha et al. 2023a).

The liquefaction degree calculated from the model output and observations indicate that sediment failure occurred near the shallow quadpod during the second wave event when the shallow quadpod settled into the sediment. A liquefaction degree map was computed from the model output, showing areas with a higher likelihood of seafloor instability and the predicted failure depth in areas where the liquefaction may occur. Moreover, the relative water depth presented a prominent influence on the failure depth, with no liquefaction expected for relative water depths greater than 0.25 for the observed stormy conditions and greater than 0.42 for simulated conditions with boundary conditions set as H_s=3 m and T_p=7 sec.

These results are consistent with the hypothesis that both liquefaction and sediment accretion occurred during the field experiment. Furthermore, it builds upon previous research by allowing morphological evolution and liquefaction analyses to be conducted throughout the area of interest rather than being constrained by the location of observation stations, which has important implications for seafloor instability study and object burial during stormy conditions.

4.3. Sand Wave Migration

We identified the sand waves of approximately 2 m in height to migrate nearly 40 m with counterclockwise rotation between two bathymetric surveys (Figure 6) performed three months apart near the Wasque Shoals, about 1 km from the southeastern corner of Martha's Vineyard,

Massachusetts. The region is characterized by strong tidal currents, intermittent energetic surface wave events, and shallow water with local depth ranging from 2 to 7 m. We used the Delft3D, with a three-dimensional approach to examine the sand wave dynamics by incorporating surface waves, winds, currents, and bathymetric observations. The model successfully simulates sand wave migration in comparison to observations. Model sensitivity analyses show that the sand wave migration reduces by 65% with the absence of the surface waves. The modeled sand wave migration speed is correlated with the tidal current Shields parameter, and sharp increases in migration speed occur when the wave-driven Shields parameter increases in response to energetic surface wave events. The combined effect of tides, surface waves, and bathymetry is the origin of the rotational aspect of the sand wave, using the Shields parameter as an indicator of tidal currents and surface wave influence on sand wave dynamics. Detailed information can be found in the following paper:

Pessanha, V.S., P.C. Chu, M.K., Gough, and M.M. Orescanin, 2023b: Sand wave migration near the southeastern corner of Martha's Vineyard, Massachusetts, USA. *International Journal of Sediment Research*, **38**, https://doi.org/10.1016/j.ijsrc.2023.04.006

4.3.1. Delft3D Model Setup

The model comprises two domains coupled using the offline nesting modeling approach to improve the spatial resolution (Figure 5). The overall domain (coarse resolution) is modeled to provide (offline) boundary conditions for the nested domain (finer resolution). Once the boundary conditions have been created, simulations using the nested domain can be run independently of the overall domain, reducing the computational cost.

The overall domain uses the two-dimensional horizontal (2DH) model approach with one vertical layer (depth-averaged mode). The flow coarse grid (Figure 5a), with a resolution varying from 1 km to 40 m (in the study area), stretches 40 km north and south and 55 km east and west. The wave coarse grid (86 km in the north-south direction and 80 km in the east-west direction) has a resolution of 1 km, the wave intermediate grid resolution is 200 m, and the wave fine grid resolution is 40 m. Similar to Roelvink & Walstra (2005), the wave model grids cover a larger area than the flow grids preventing boundary disturbances of the wave model from entering the flow domain. In addition, the boundary conditions of the overall domain were defined at the outer boundaries of the flow coarse grid and driven by tidal water level variations calculated using the global inverse solution from altimetry data with the 13 main astronomic constituents, including M2, S2, N2, K2, O1, and K1. The significant wave height, wave period, wave directions, and directional spreading were used to create wave boundary conditions based on observations from NOAA buoy station 44097, located in the 50-m water depth (Figure 5a). On all open boundaries (wave coarse grid), these parameters were applied uniformly. Moreover, bathymetric data from the U.S. Coastal Relief Model (NOAA/NGDC, 1999), with 90 m resolution, were used in the overall domain that was not covered by the bathymetric survey conducted during the field experiment. The time step was chosen at 9 seconds based on the Courant–Friedrichs–Lewy (CFL) number. Default values of the Delft3D model were applied for the Chézy bottom roughness (65 $m^{1/2}/s$) and horizontal eddy viscosity (1 m^2/s). In addition, the flow and wave modules coupling time was adjusted to 60 minutes. The bottom friction component of wave dissipation with constant

bottom friction was calculated using the JONSWAP model (Hasselmann et al. 1973).

A three-dimensional (3D) model with a non-orthogonal grid that accounts for suspended sediment transport and is capable of accurately predicting bedforms was presented by Fang and Wang (2000) and Fang and Rodi (2003). Following their path, the detailed domain employs the 3D model approach to examine the sand wave dynamics affected by three-dimensional processes. The flow detailed grid (Figure 5b) covers the study area with 8 m horizontal resolution and 20 non-equidistant vertical σ-layers, with resolution in terms of the percentage of the water depth. The first 5 layers (closer to the seabed) have the highest resolution, 2% of the water depth. The following 12 layers have a resolution of 5%, and the last 3 layers (closer to the surface) have a resolution of 10% of the water depth. The model used the Riemann boundary conditions on the 4 open boundaries at the detailed domain to include tidal current, allowing the outgoing waves to pass the open boundary without reflecting into the computational domain. The sediment transport, including bed load and suspended load transport, and morphological evolution were computed only in the flow detailed grid to allow the comparison with field measurements. Default values of the Delft3D model were applied for the initial bed of sediment (5 m), initial water level (zero m), and a spin-up interval (720-minute) to avoid any impact from an initial hydrodynamic instability on the bottom change computation. The eddy viscosity was computed using the k-ε turbulence model. Moreover, data from the bathymetric survey conducted on 10 October 2013 was set as initial bathymetry. Based on the CFL number, a time step of 6 seconds was established. The sand was chosen as the sediment type, with a median grain size (D_{50}) of 500 μm (Hopkins et al., 2018) and a sediment-specific density of 2,650 kg/m^3. The wind input files were set up using observations from the Air-Sea Interaction Tower (ASIT), Martha's Vineyard Coastal Observatory (MVCO: https://mvco.whoi.edu), located 3 km south of Martha's Vineyard in 17-m depth (Figure 5b).

4.3.2. Model Calibration and Validation

The model results using the set-up described in section 3.3.1 were compared to the MVCO 12-m underwater node observations for a period of one month. Figure 17 indicates a good model-data agreement for mean water level (*MWL*), significant wave height (H_s), and mean current velocity (V), with positive values of V representing the flow moving in the flood tide direction, and negative values the flow moving in the ebb tide direction. Since the model produced satisfactory results for *MWL* (SS=0.988), V (SS=0.971), and H_s (SS=0.959), calibration was performed with respect to morphology.

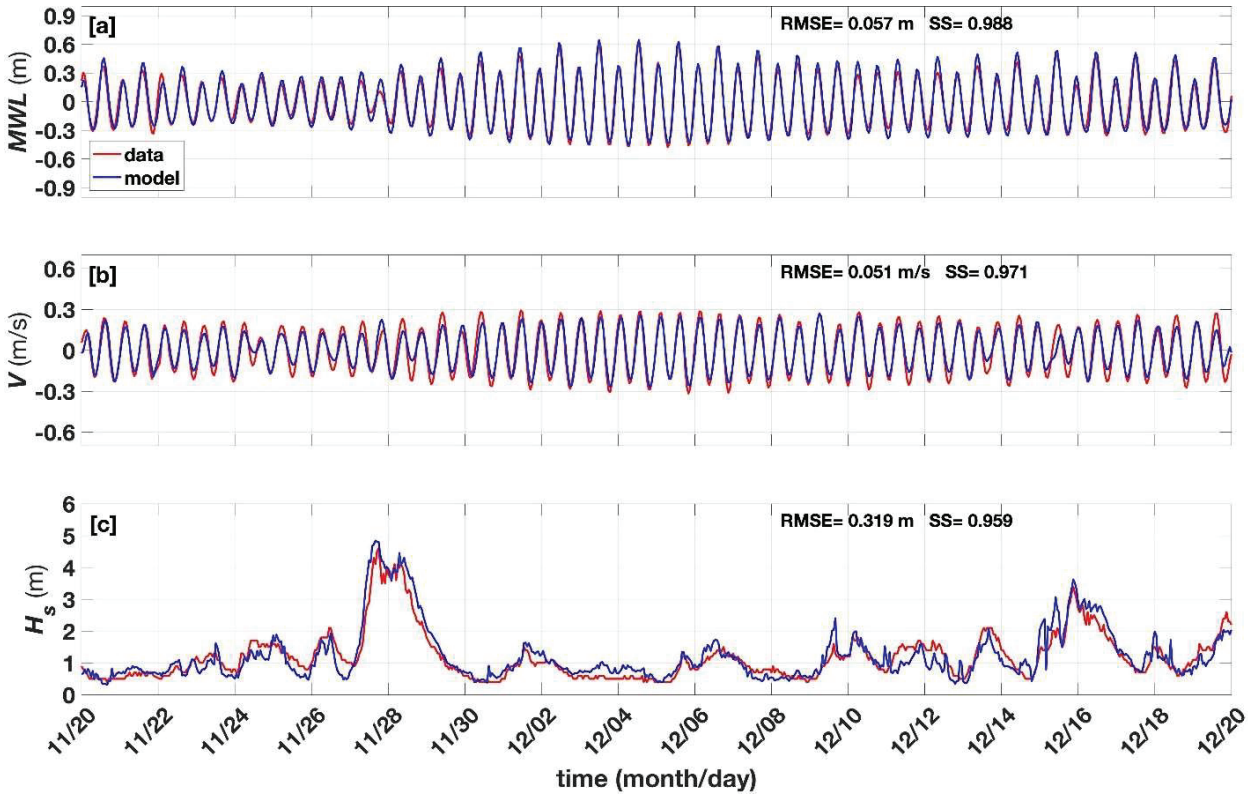

Figure 17. Model calibration for hydrodynamics. Comparison between model results (blue) and observations at the MVCO 12-m underwater node (red) for (a) mean water level (*MWL*), (b) depth-averaged current (*V*) with positive values indicating the flow moves in the flood tide direction and negative values denoting the flow moves in the ebb tide direction, and (c) significant wave height (H_s). The root mean square error (RMSE) and skill score (SS) for each comparison are provided in the upper right of the panels (from Pessanha et al. 2023b).

The calibration was conducted by tuning the user-defined bed slope parameter (α_{BS}) to adjust the correction factor for the bed slope effects (α_S). This parameter accounts for the effect of the bed slope in bedload transport and must be calibrated to adequately predict the sand wave migration (Wang et al., 2019). Higher values of α_{BS} produce a stronger bed slope effect, decreasing upslope and increasing the downslope sediment transport. The model result was compared with observed bathymetry along the calibration transect (160 m length) depicted in Figure 6, which is oriented in the mean flow direction. The parameter α_{BS} =0.2 achieved the best result with BSS=0.916. Figure 18 shows the model result for different values of α_{BS} (0.1, 0.2, 0.5, and 1) considering the observed bathymetry and summarizes the results along the calibration transect.

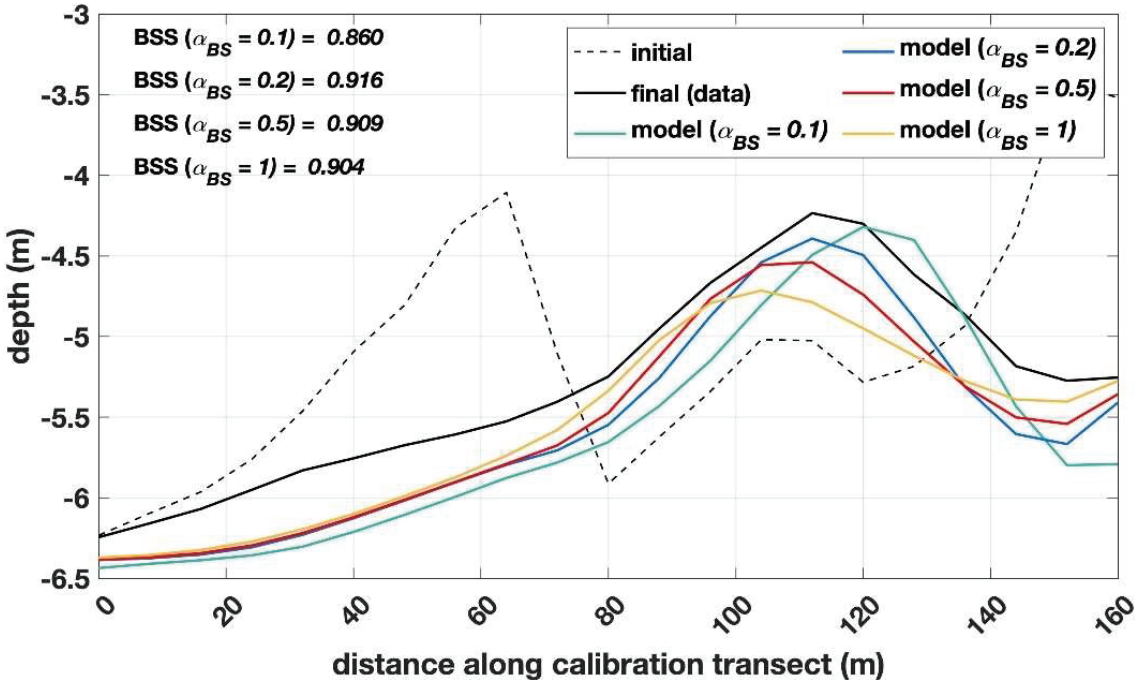

Figure18. Model calibration for morphology. Bed level profiles along the calibration transect (shown in Figure 6). Comparison between model results for different values of bed slope parameter α_{BS} (0.1, 0.2, 0.5, and 1) and observed bathymetry. The Brier skill score (BSS) for each model result in comparison with the observed bathymetry is provided in the upper left of the panel (from Pessanha et al. 2023b).

The model was implemented in a region of complex hydrodynamics and bathymetry using a realistic approach that implements observations as input instead of an idealized model, requiring the need for model validation by comparing results to field observations. The *MWL*, *V*, and H_s observed at quadpod location were compared with the model output for a period of 50 days (Figure 19). The *MWL* was predicted by the model (Figure 19a) with the calculated SS (0.979) and RMSE (0.066 m). In Figure 19b, *V* is represented by positive values when the flow moves in the flood tide direction and negative values when the flow moves in the ebb tide direction. The SS of *V* was calculated as 0.816 and the RMSE as 0.074 m/s. For H_s (Figure 19c), the SS was calculated as 0.962 and the RMSE as 0.131 m.

To qualitatively assess the model results, the bathymetric changes were calculated by subtracting the initial bathymetry from the observed and simulated final bathymetry. Figure 20 presents the respective observed and simulated bathymetric change maps showing the location of sediment accretion (in yellow) and erosion (in blue). The model result closely reflects the observed pattern of changes, with erosion in the areas where sand wave crests existed and sediment deposition in the areas where the initial bathymetry presented troughs.

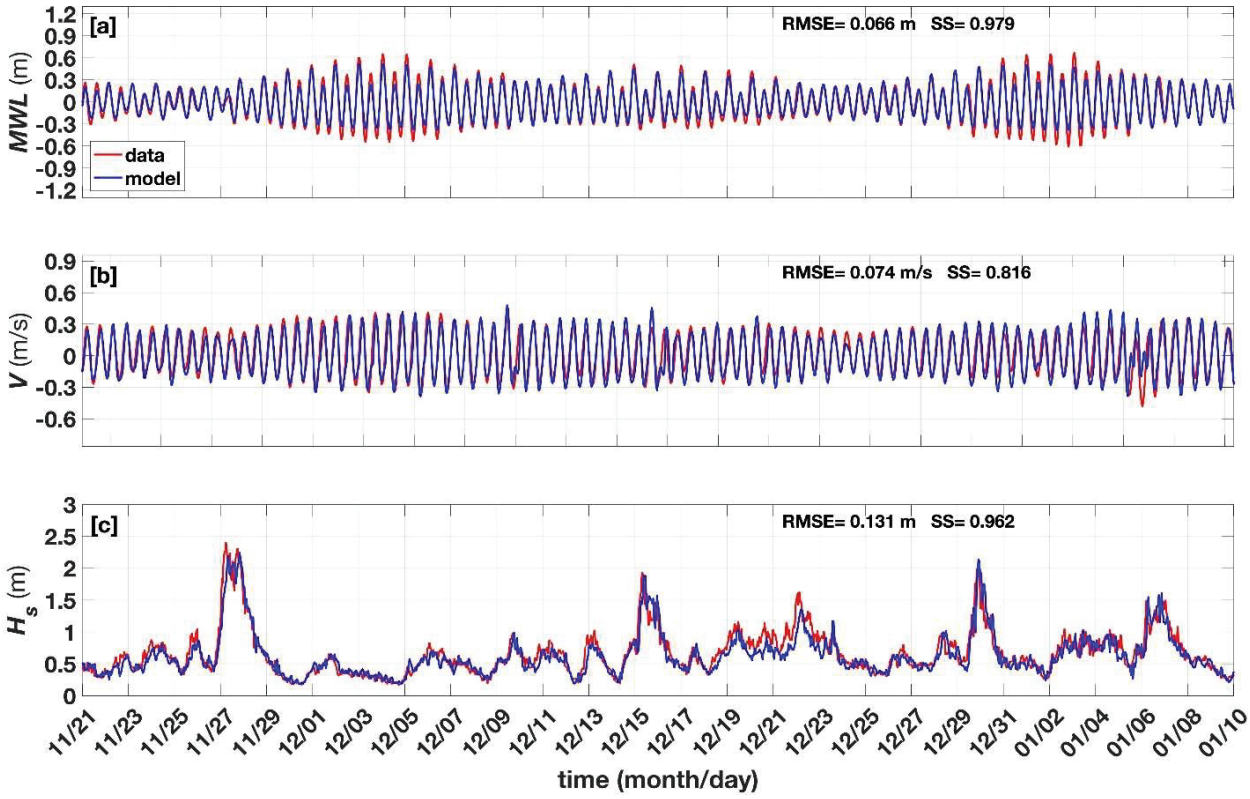

Figure 19. Comparison between model results (blue) and observations (red) at the quadpod location for (a) mean water level (*MWL*), (b) depth-averaged current (*V*) with positive values indicating the flow moves in the flood tide direction and negative values denoting the flow moves in the ebb tide direction, and (c) significant wave height (H_s). The root mean square error (RMSE) and skill score (SS) for each comparison are provided in the upper right of the panels (from Pessanha et al. 2023b).

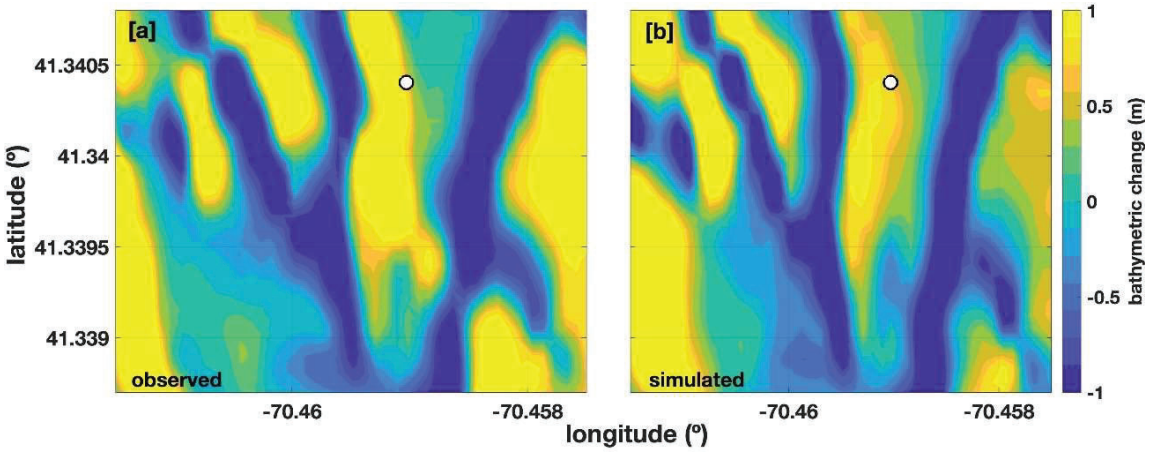

Figure 20. (a) Observed and (b) simulated bathymetric change considering the difference between the initial (16 October 2013) and final (10 January 2014) bathymetry. Yellow is sediment accretion, and blue is erosion. The white dot shows the position of the quadpod (from Pessanha et al. 2023b).

Furthermore, the model performance was evaluated by comparing simulated and observed final bathymetry along seven transects (Figure 21a). These parallel transects are oriented in the mean flow direction and separated by 20 m from each other. Each transect is 160 m long and composed of 21 points equally spaced by 8 m (model spatial resolution), totaling 147 points considering all transects. Figure 21b shows a scatter plot comparing the observed and predicted depth for these 147 points. The model adequately simulated the seabed evolution with a mean BSS of 0.862 (considering all transects).

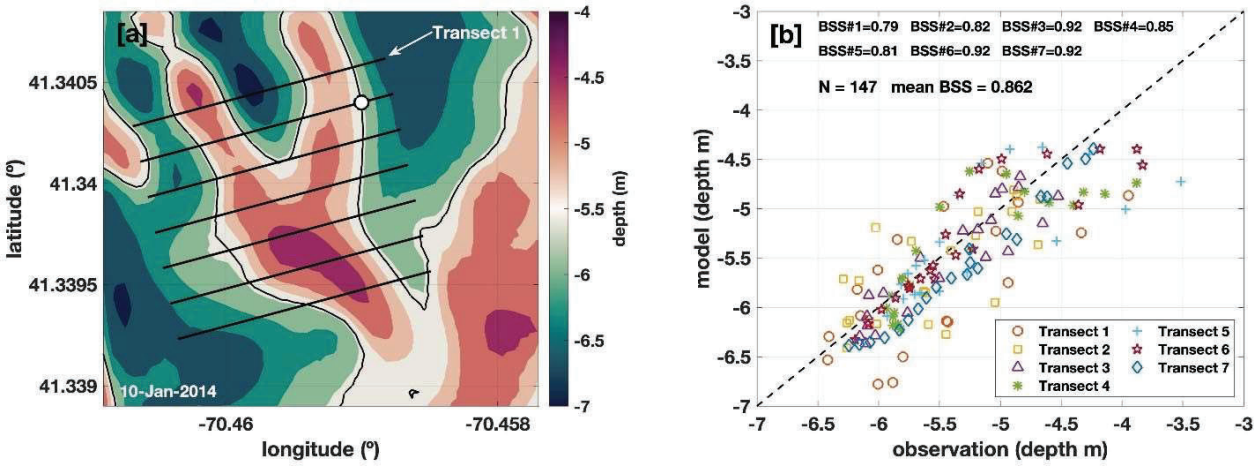

Figure 21. (a) Model predicted bathymetry and (b) comparison to the observed bathymetry on10 January 2014. The seven transects and the quadpod location in (a) are represented by the black lines and white circle, respectively. The 1:1 ratio line is represented by the black dashed line. The Brier skill score (BSS) for model results in comparison with the observed bathymetry for each transect is provided in (b), as the number of points considered and the mean BSS (from Pessanha et al. 2023b).

4.3.3. Sand Wave Migration due to Tidal Currents and Surface Waves

During the 3-month simulation, the model produced hourly bathymetric maps from 16 October 2013 to 10 January 2014. For each hour, a seabed profile along transect 2 is determined from each bathymetric map from which hourly sand wave migration distance and speed toward the northeast direction can be estimated (Figure 22a). The influence of tidal current and surface wave on sand wave migration is evaluated by comparing (Figure 22b) dimensionless Shields parameters for both tidal currents (θ_t) and surface waves (θ_w),

$$\theta_t = \frac{\tau_t}{(\rho_s - \rho_w)\, g d_{50}}, \qquad \theta_w = \frac{\tau_w}{(\rho_s - \rho_w) g d_{50}} \tag{32}$$

to the critical Shields parameter (θ_{cr}) (Shields 1936). The migration speed, θ_t, and θ_w presented in Figure 22 are computed using the model result at the quadpod location. The shear stress for tidal currents (τ_t) and surface waves (τ_w) are calculated following van Rijn (1993),

$$\tau_t = \rho_w g \left[\frac{V}{18\log_{10}\left(4.8d / d_{50}\right)} \right]^2, \quad \tau_w = \rho_w u_{orb}^2 \exp\left[5.213\left(\frac{2.5d_{50}}{A_{orb}} \right)^{0.194} - 5.977 \right] \tag{33}$$

where V is depth-averaged tidal current; ρ_s is the density of the sediment; ρ_w is the density of sea water; g is the gravitational acceleration; d is the local depth; U_{br} is the wave orbital velocity, and A_{orb} is the wave orbital excursion near bed.

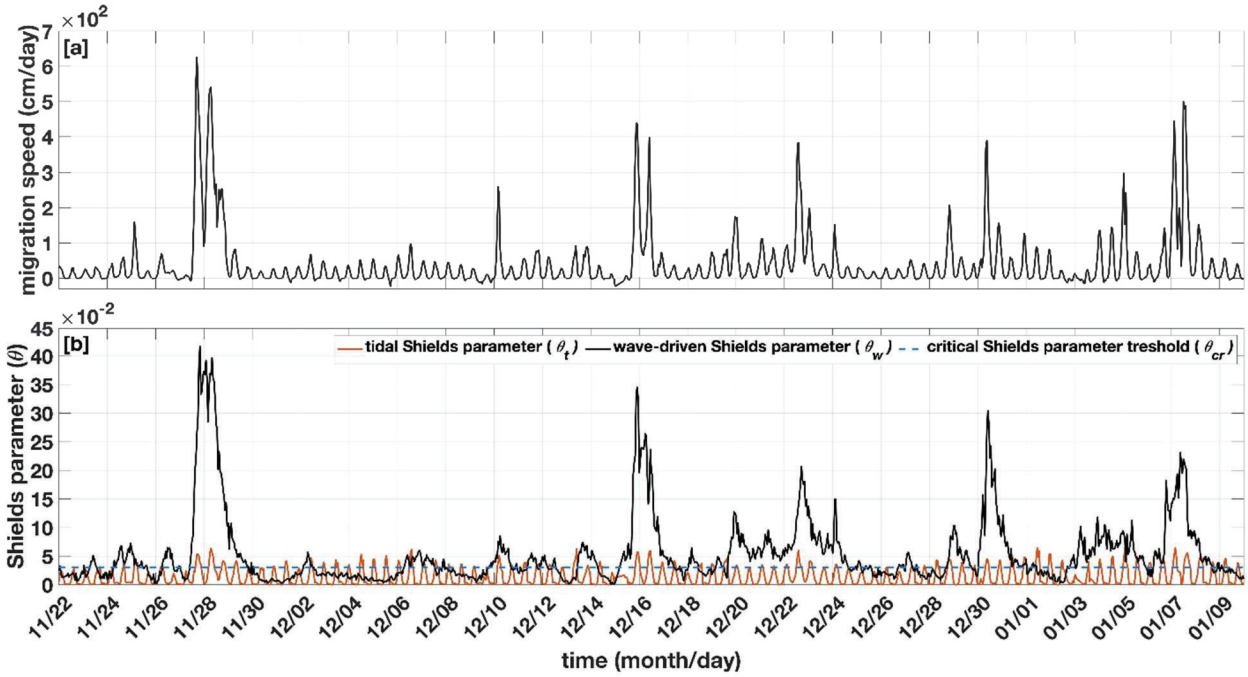

Figure 22. (a) Hourly mean migration speed, (b) wave-driven Shields parameter (θ_w), and tidal current Shields parameter (θ_t) time series. The blue dashed line represents the critical Shields parameter (θ_{cr}) for initiation of sediment motion (from Pessanha et al. 2023b).

The average migration speed over the 3-month model simulation is 40.4 cm/day along transect 2 and 55.8 cm/day along transect 7, which is consistent with the sand wave migration observed in the bathymetric data and with the observed mean migration speed of 50 cm/day over a 9-month period, from 16 October 2013 to 18 July 2014, reported by Jones & Traykovski (2019). However, the estimated migration speed is not constant as large peaks in migration speed can be observed to occur on 28 November,16, 22, and 30 December, and 7 January (Figure 23a). The peak migration speed is estimated as high as 627.3 cm/day and reaches over 200 m/s on multiple occasions. The regularly spaced smaller peaks are related to θ_t and migration driven by the tidal currents. A qualitative comparison between mean migration speed and Shields parameter (Figure 23b) indicates that peaks of estimated migration speed correspond to peaks of θ_w, which also coincide with periods of wave events when H_s >1.5 m (Figure 19c), which highlight the influence of surface waves on the sand wave migration speed.

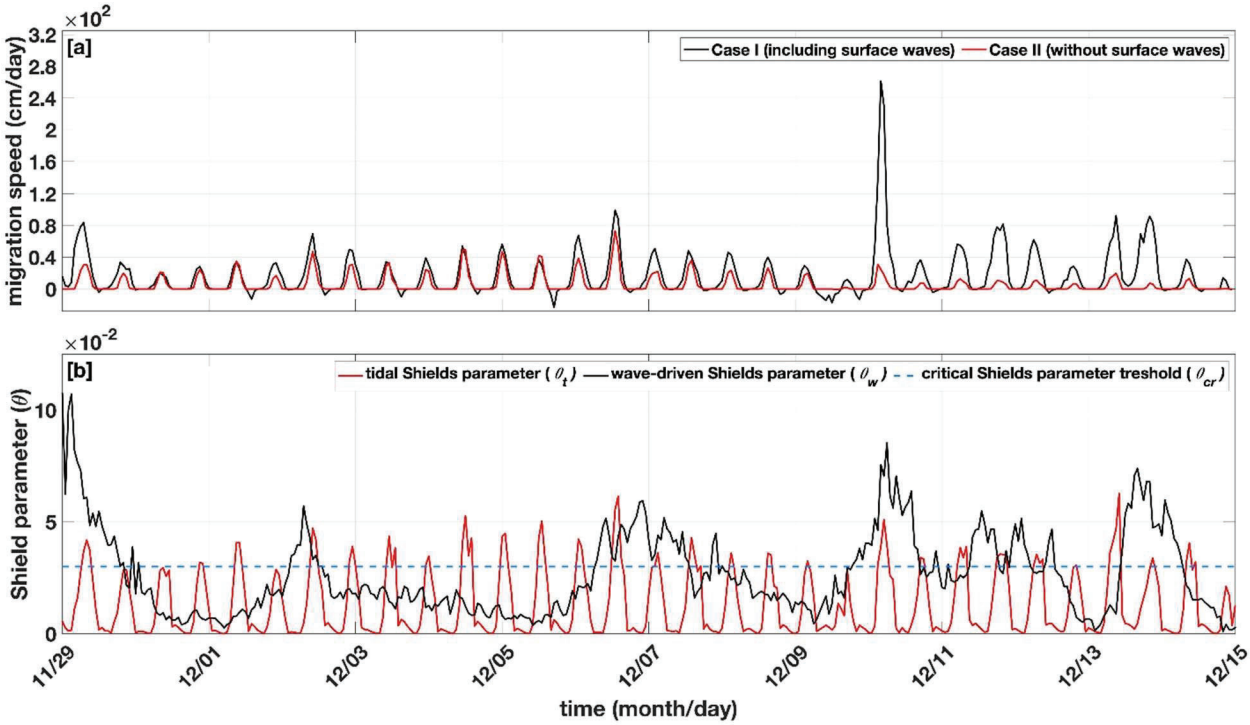

Figure 23. (a) Hourly mean migration speed, (b) wave-driven Shields parameter (θ_w), and tidal current Shields parameter (θ_t) time series estimated from model results in a period (16 days) of no large surface wave event. The blue dashed line represents the critical Shields parameter (θ_{cr}) for initiation of sediment motion. The mean migration speed was estimated from a simulation including surface waves (black curve) and from a simulation without surface waves (red curve) (from Pessanha et al. 2023b).

From 29 November to 15 December 2013 (16 days), no large surface wave events occurred (H_s < 1 m with mean H_s = 0.467 m, see Figure 19c), which is reflected in the relatively small θ_w during this time (Figure 23b). Figure 23a zooms in on the hourly mean migration speed estimated from a simulation including surface waves (back curve) and a simulation without surface waves (red curve) during this time. The simulation, including surface waves, presented an average migration speed of 17 cm/day, consistent with field observations of 12 ± 3.6 cm/day (95% confidence interval) estimated from a rotary side-scan sonar data in this exact location and period (Jones & Traykovski, 2019). For the simulation without surface waves, the average migration speed is 5.6 cm/day, representing a reduction of 67% in the average migration speed when surface waves are taken into consideration. The migration speed and θ_t are correlated in simulations with and without surface waves, with correlation coefficient (R) of 0.70 and 0.72, respectively. Peaks of migration speed in the simulation accounting for surface waves corresponds to periods in which θ_w is greater than the θ_{cr} (Figure 23b).

According to Campmans et al. (2018), although surface wave events do not trigger sand wave migration, they can boost the migration of sand waves in the presence of asymmetrical tidal flow, decreasing sand wave growth and eventually reducing sand wave height. These conclusions come from simulations using a highly idealized 2DV model considering storm conditions in a region

with a mean water depth of 30 m. However, when they modeled sand wave migration for a more realistic scenario with surface waves in brief intervals of stormy conditions alternating with periods of good weather conditions, the results are similar to the simulations for sand wave migration considering only tidal forcing. In contrast, the result presented in Figure 23 implies that the influence of surface waves on shallow areas (water depth less than 10 m) is relevant even during less energetic periods.

4.3.4. Rotation of the Sand Waves

The comparison between the observed initial and final bathymetry (Figure 6) exhibits counterclockwise sand wave rotation where the southern portion of the sand wave migrates faster than the northern portion. Figure 24 presents a comparison between two simulations, the first including surface waves (case I) and the second a simulation without surface waves (case II) along transect 1 (northern portion of the sand wave) and transect 7 (southern portion). For case I, the sand wave migration along transect 7 is 48 m (distance between the black and blue arrow), which is 16 m further than the migration on transect 1 (32 m). Both transects for case II underestimated the migration and sand wave rotation, as evidenced by the decreased migration, distance between the black and red arrow, on transects 1 (12 m) and 7 (16 m).

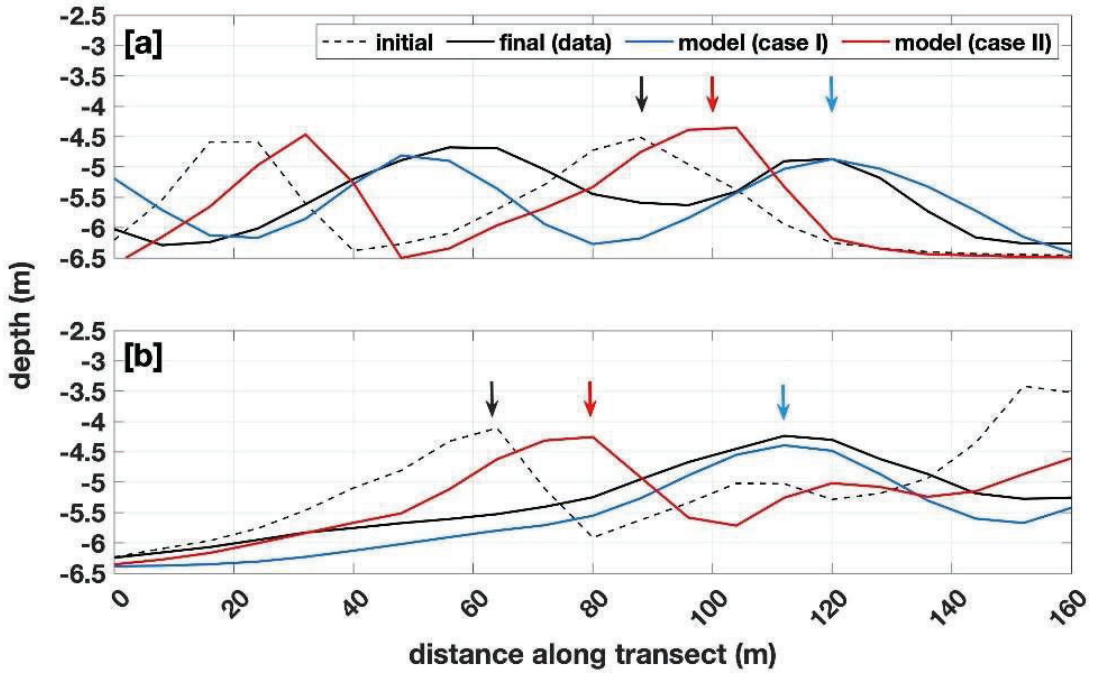

Figure 24. Bed level profiles along (a) transect 1 and (b) transect 7. Bathymetry on 16 October 2013 and 10 January 2014 are shown as dashed black and solid black curves, respectively. The blue line represents the model result for case I, including surface waves, and red line, for case II, simulation without surface waves. The black arrow indicates the observed initial position of a sand wave peak, blue and red arrows indicate the modeled final position of the same sand wave peak for case I and case II, respectively (from Pessanha et al. 2023b).

Sand wave rotation has been attributed to spatially changing migration speeds related to depth since migration speeds tend to be slower in deeper locations and faster in shallower areas, which tilt the original sand wave axis (Tonnon et al., 2007). In shallow areas, the flow acceleration owing to the energy conservation enhances the spatial tidal flow variation impacting sand wave migration speed along with the sand wave rotation. A similar effect on the spatial variation of sand wave migration speed is caused by the orbital motions from surface waves which stir up the sediment at the seabed in shallow areas when surface waves are sufficiently vigorous (Tonnon et al., 2007); this stirring can amplify the migration (Campmans et al., 2018). The Shields parameters (θ_w and θ_t) were calculated over the area of interest to examine the impact of tidal current and surface waves on the sand wave migration and rotation. Figure 25 shows θ_w maps for wave event condition (H_s = 2.4 m) and small wave condition (H_s = 0.5 m), and θ_t maps for maximum tidal conditions (V = 0.41 m/s) during the spring tidal conditions and mean tidal conditions, considering the average of peak tidal current (V = 0.28 m/s). The highest values of θ_w and θ_t are reached for wave event and maximum tidal conditions, in which Shields parameter exceeds the θ_{cr} in the entire area of interest (Figures 25a and 25c). In contrast, θ_w and θ_t do not surpass the θ_{cr} values in areas highlighted in gray (Figures 25b and 25d) for the small wave and mean tidal conditions. All maps exhibit higher values of Shields parameter to the south, where higher migration speed is observed. These results reveal that the combined effects of tidal flow and surface waves cause a faster migration speed in the southern portion, forcing the sand wave to rotate counterclockwise.

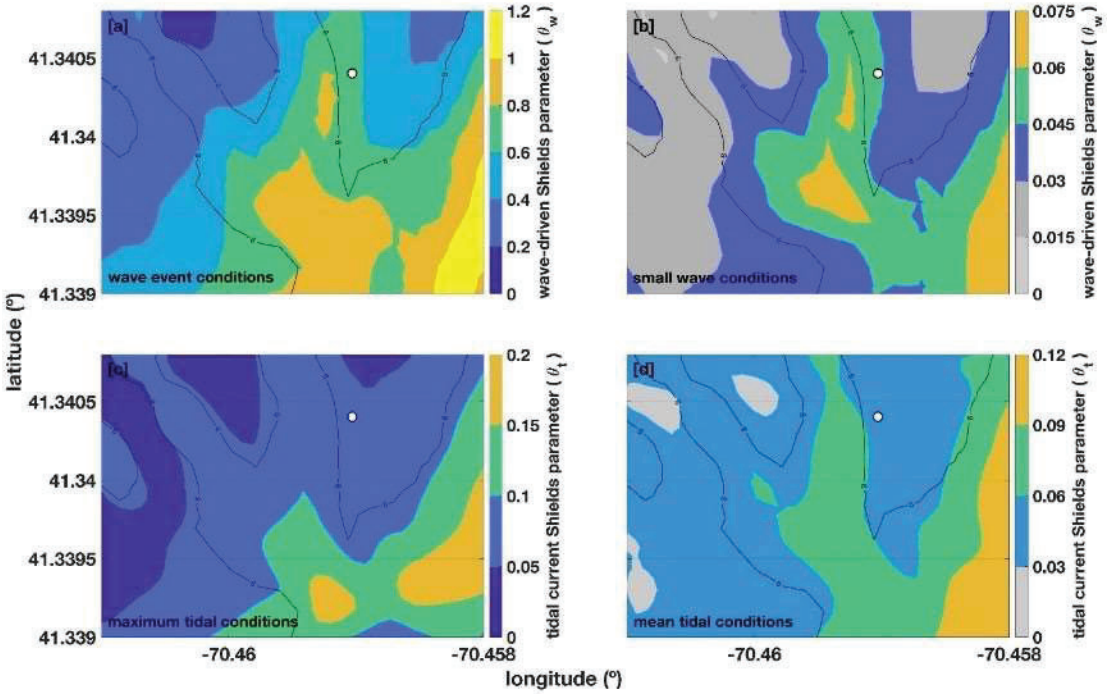

Figure 25. Wave-driven Shields parameter (θ_w) for (a) wave event (H_s = 2.4 m) and (b) small wave (H_s = 0.5 m), and tidal current Shields parameter (θ_t) for (c) maximum tidal conditions (V = 0.41 m/s) and (d) mean tidal conditions (V = 0.28 m/s). The 6 m depth contour is represented by the black line and the quadpod location is denoted by the white dot (from Pessanha et al. 2023b).

4.4. Coupled Delft3D-UnMUMB Modeling

Coupled Delft3D-UnMUMB model has been developed to predict munition's mobility and burial on sandy seafloor. The Delft3D model is used to predict seabed environment such as currents, waves (peak wave period, significant wave height, wave direction), water level, sediment transport, and seabed change, which are taken as the forcing term to the UnMUMB model consisting of three components: (a) munition's physical parameters such as diameter, length, mass, and rolling moment, (b) dynamics of rolling munition around its major axis, and (c) parameterized sediment scour model with re-exposure. The model is compared with the observational data collected from a field experiment (TREX13) from 21 April to 13 May 2013 off the coast of Panama City, Florida funded by the Department of Defense Strategic Environmental Research and Development Program. The experimental data contain both objects' mobility using sector scanning sonars and maintenance divers as well as simultaneous environmental time series data of the boundary layer hydrodynamics and sediment transport conditions. Comparison between modeled and observed data clearly show the model capability and limitation. Detailed information can be found in the following two papers:

Chu, P.C., C.W. Fan, J. Calantoni, and A. Sheremet, 2022: Prediction of mobility and burial of objects on sandy seafloor. *IEEE Journal of Oceanic Engineering*, **47**, No. 1, 2022. https://ieeexplore.ieee.org/stamp/stamp.jsp?arnumber=9552391&tag=1
Chu, P.C., V.S. Pessanha, C.W. Fan, and J. Calantoni, 2021: Coupled Delft3D-object model to predict mobility of munition on sandy seafloor. *Fluids*, **6** (9), 330, https://doi.org/10.3390/fluids6090330.

4.4.1. Delft3D Model Setup

Two grids with different grid cell sizes were nested (Figure 26) to create a region with finer resolution. These rectangular grids compose the flow domain. The flow outer grid (coarser resolution) is composed by 137×75 grid points spacing of 50 m both longshore and cross-shore directions. The flow inner grid (finer resolution) grid has 20 m resolution and was divided into 139× 124 grid points equally spaced. The sediment transport and morphological evolution were computed only in the flow inner grid. The wave domain (Figure 26) is defined to avoid the boundary effect and allow the use of deep quadpod data to set up the wave boundary conditions. The wave grid is composed by 273×111 grid points with 50 m resolution. The bathymetric data (Figure 26) was from the Northern Gulf Coast Digital Elevation Model from the National Oceanic and Atmospheric Administration/National Geophysical Data Center (NOAA/NGDC) (see the website: https://catalog.data.gov/dataset/northern-gulf-coast-digital-elevation-model156ed). The resolution of this data set varies between 1/3 arc-second and 1 arc-second (around 10 and 30 m). The time step is set as 0.2 s for the coarse domain (grid size 50 m) and 0.1 s for the finer domain (grid size 20 m). The small time-steps (0.2 s, 0.1 s) are needed to satisfy the Courant-Friedichs-Lewy (CFL) condition of computational stability for the Delft3D flow module.

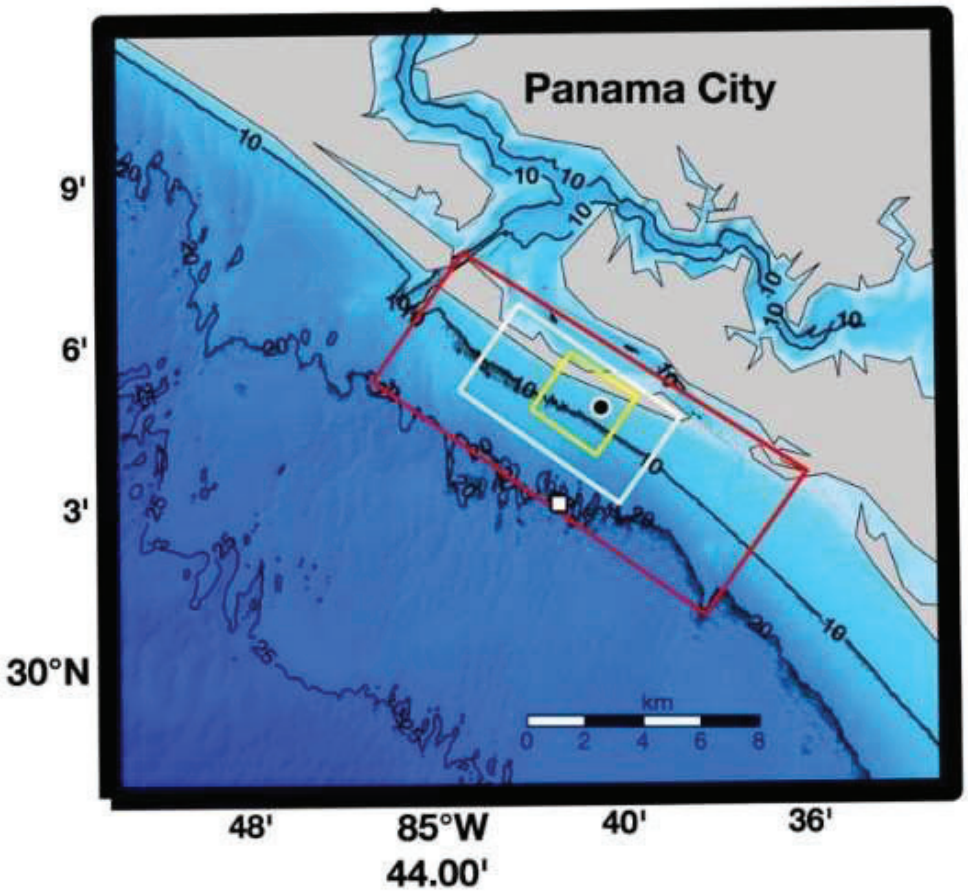

Figure 26. Study area with bathymetry, depth contours (10 m, 20 m, and 25 m), and computational grids for wave module (red), flow module with coarse resolution (white), and flow module with fine resolution (yellow). The black dot represents the shallow quadpod location, and the white square denotes the deep quadpod location (from Chu et al. 2021).

The wind input files were set up using the ERA5 Reanalysis data from the European Centre for Medium-Range Weather Forecasts (ECMWF), with 0.25° resolution (see the website: https://rda.ucar.edu/datasets/ds633.0) for the flow and wave modules. The Global Inverse Tide Model TPXO 8.0 with 1/45-degree resolution was used to create the boundary conditions for the flow module. For the alongshore boundary, the water level with astronomic forcing was imposed. The water level gradient (Neumann boundary condition) was chosen with a constant zero water level slope in the longshore direction for both across-shore open boundaries. It allows for flow to leave and enter the lateral boundaries with no spurious circulation.

As an initial condition, the water level and current velocity were set to zero. Additionally, the sediment transport boundary conditions were set by specifying the inflow concentration as zero kg/m^3. The initial condition for the sand sediment was set as a uniform zero concentration, and the initial bed of sediment was set to 5 m. Wave boundary conditions were set based on the measurements from the deep quadpod location using the significant wave height, wave period, wave directions, and directional spreading. These parameters were applied uniformly on the three open boundaries. The spin-up interval of 720 minutes was established to prevent any influence of a possible initial hydrodynamic instability on the bottom change calculation, which starts only after the spin-up interval. The sediment type was set as sand with a sediment-specific density of 2,650 kg/m^3.

4.4.2. Delft3D Model Output

The Delft3D output data with 1-hour resolution are used as input to the object model. The output from the flow module includes the water depth (h) and the current velocity, $\mathbf{U}_c = \mathbf{i}v_e + \mathbf{j}v_n$, with ($\mathbf{i}$, $\mathbf{j}$) the unit vectors in longitudinal and latitudinal directions, and $U_c = (v_e^2 + v_n^2)^{1/2}$ the current speed. The output from the wave module includes the wave peak-period (T_P), significant wave height (H_S), wave direction, and bottom wave orbital velocity (U_{br}). The bottom water velocity vector of combined current and waves is represented by $\mathbf{V}_w$ with $|\mathbf{V}_w| = U_c + U_{br}$ and the orientation, $\psi = \tan^{-1}(v_n/v_e)$. Figure 27 shows the time series of the environmental parameters [v_e, v_n, h, T_P, H_S, U_{br}] predicted by the Delft3D (red curve) and observed by the AWAC (black curve). The AWAC only provides the observed data for [v_e, v_n, h, T_P, H_S], but not the bottom orbital velocity U_{br}, which was calculated using a well-established linear wave model with Matlab function (Wiberg and Sherwood 2008) with the observed water depth (h), significant wave height (H_S), and peak period (T_p).

Since the munitions were found totally buried without mobility in the morning of 8 May 2013 by the divers in the TREX13 and the TREX13 provides munitions' mobility information from 21 April to 7 May 2013, the integration period for the coupled Delft3D-object model was set as 21 April – 7 May 2013. The root-mean-square error (RMSE) between the Delft3D output and the TREX13 observations is 0.105 m for the water level, 0.111 m/s for the east-west current speed, 0.0641 m/s for the north-south current speed, and 0.0946 m for the significant wave height, and 0.0928 m/s for the bottom wave orbital velocity. The Bias between the Delft3D output and the TREX13 observations is -0.0244 m for the water level, -0.0367 m/s for the east-west current speed, 0.0055 m/s for the north-south current speed, and 0.0429 m for the significant wave height, and -0.0786 m/s for the bottom wave orbital velocity. The correlation coefficient between the Delft3D output and the TREX13 observations is high as 0.966 for the significant wave height, 0.941 for the bottom wave orbital velocity, reasonably high as 0.796 for the water depth, as 0.571 for the north-south current speed, and 0.551 for the east-west current speed, and the lowest as 0.373 for the peak wave period. The performance of the Delft3D modeling is reasonably well according to the criteria presented in van Rijn et al. (2003).

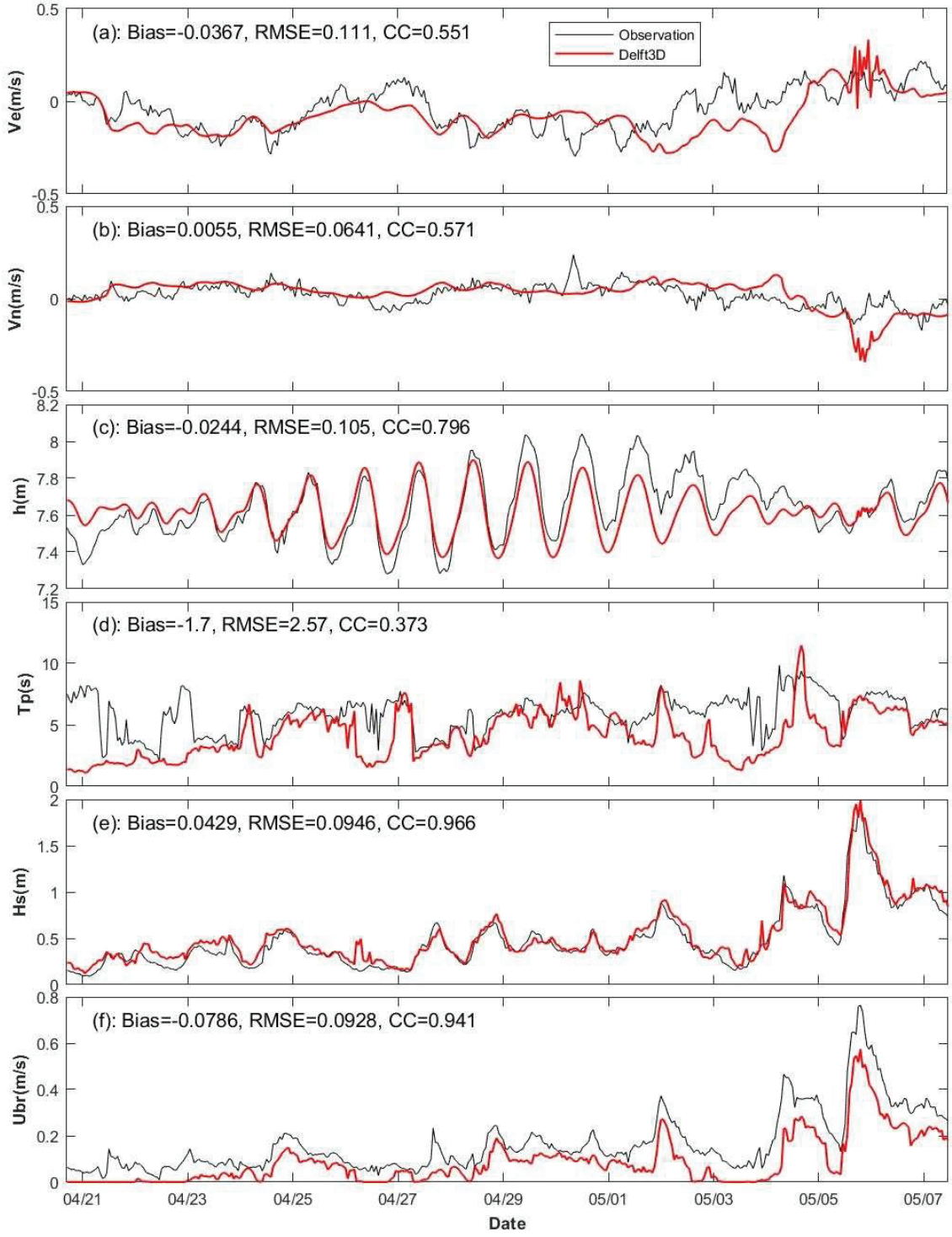

Figure 27. Comparison of Delft3D predicted (red) and observed during the TREX13 (black) at the shallow quadpod from 21 April to 7 May 2013: (a) near bed (~0.15 m) longitudinal current v_e (m/s), (b) near bed (~0.15 m) latitudinal current v_n (m/s), (c) water depth h (m), (d) peak period T_P (s), (e) significant wave height H_S (m), and (f) computed bottom wave orbital velocity U_{br} (m/s) (from Chu et al. 2021).

4.4.3. Sediment Shields Parameter

Use of the wave data (T_P, U_{br}) from Figures. 6e and 6g, and sediment parameters (ρ_s= 2.69×103 kg/m^3, d_{50}=0.23×10^{-3} m) from the TREX13 [9][13], the sediment Shields parameter (θ_{sed}) are calculated from 21 April to 7 May 2013. It is less than 0.1 all the time except an atmospheric cold fronts passing by on 05-06 May 2013. The maximum value of θ_{sed} reached 0.33 (Figure 28).

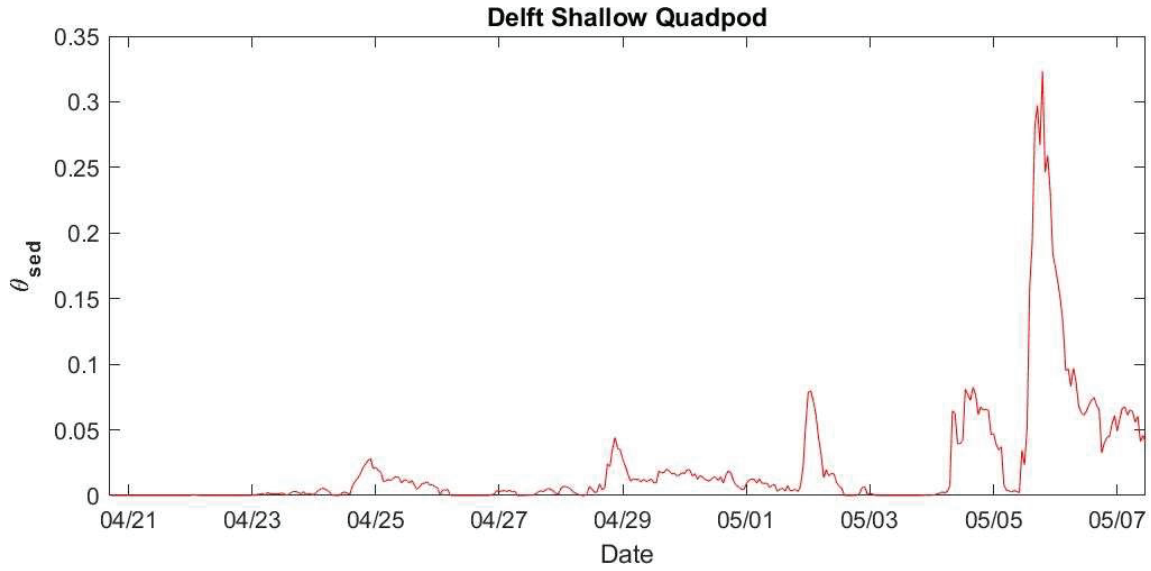

Figure 28. Time series of sediment Shields parameter (θ_{sed}) at the shallow quadpod computed from the Delft3D model output (from Chu et al. 2021).

With the bottom wave orbital velocity (U_{br}), sediment density(ρ_s), medium grain size (d_{50}), and in turn the sediment Shields parameter (θ_{sed}), the equilibrium object percentage burial ($p_{B,eq}$) are calculated using (9) with coefficients $a_1 = 1.6$, $a_2 = 0.85$, $a_3 = 0$. It is noted that the predicted burial percentage (p_B) represents the depth that an object on the surface would be buried to at that moment. But an object deployed at the beginning of the time sequence would always remain buried at the deepest burial it has reached so far. The burial depth of the base of the object below the ambient seabed is equivalent to the greatest depth that the scour pit has reached up to that point in time (Trembanis et al. 2007). In other words, scour only acts to bury an object deeper. It can never unbury (re-exposure). Similar to Trembanis et al. (2007), a simple parameterization was proposed by Chu et al. (2021, 2022) to represent the re-exposure process starting from k (= 1, 2, …): (a) doing nothing if $p_B(t_{k+1}) \geq p_B(t_k)$, and (b) computing the weighted average

$$\tilde{p}_B(t_{k+1}) = w p_B(t_k) + (1-w) p_B(t_{k+1}) \text{ if } p_B(t_{k+1}) < p_B(t_k) \quad (34)$$

with w the weight coefficient. In this study, we take w = 0.80.

4.4.4. Prediction of Munition's Mobility and Burial

Munitions' mobility and burial were predicted using the object mobility and burial models with

the environmental variables predicted by the Delft3D as the forcing term. The model was integrated for each surrogate (or replica) munition deployed in the shallow quadpod with its initial location and orientation (Figure 3a) from 12:40 (14:00) local time on 20 April 2013. The angle between $\mathbf{V}_w$ (data represented by the red curves in panels a, b in Figure 27) and the direction perpendicular to cylinder 's main axis is determined. The velocity vector of combined current and waves ($\mathbf{V}_w$) is then transformed into $\mathbf{V}_w = (U, V)$ with U the perpendicular component, and V the paralleling component. Component U is used in the model. The object's physical parameters such as the diameter (D), volume, mass (M), and density (ρ_o) are obtained from Table 1.

The environmental data such as the water depth (h), wave peak period (T_P), significant wave height (H_S), bottom wave orbital velocity (U_{br}) (represented by the red curves in Figure 27), sediment data (100% sand, $d_{50} = 0.23$ mm, $\rho_s = 2.69\times10^3$ kg m^{-3}), are used by the sediment scour model [i.e., Eqs.(15), (18)-(22)] to get the burial percentage $p_B(t_k)$, and in turn the relative rolling center depth $p_b(t_k)$. With object's physical parameters (D, ρ_o, M), the calculated $p_b(t_k)$, model-predicted bottom current velocity component perpendicular to the object's main axis $U(t_k)$, coefficients [$\alpha(t_k)$, $\beta(t_k)$, from Eq.(12)] for the object mobility model [i.e., Eq.(13)], the munition's displacement at the next time step $l(t_{k+1})$ can be predicted using (14).

Based on the known initial locations of the objects at the shallow quadpod (Figure 3a), the model predicts the object's burial percentage [$p_B(t_k)$] shown in Figure 29, the objects' mobility parameter for percentage burial [$\theta_{opb}(t_k)$] shown in Figure 30, and the munition's displacement [$l(t_k)$] shown in Figure 31. The burial percentages p_B for all the objects were less than 0.5 except during the storm event on 12:00 5 May to 00:00 6 May 2013 local time (Figure 29). The red color in Figure 30 shows that the object 's rolling condition [$\theta_{opb}>1$] is satisfied.

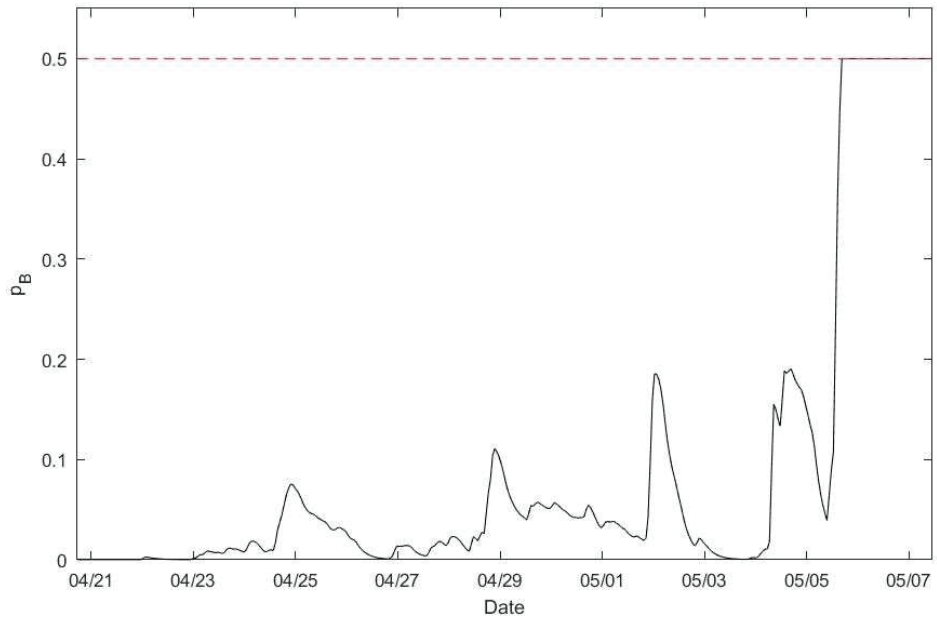

Figure 29. Model predicted burial percentage $p_B(t)$ with re-exposure parameterization [Eq.(34)] for each munition at the shallow quadpod from 20 April to 7 May 2013. The predicted burial percentage $p_B(t)$ is less than 0.5 for all the munitions during the whole time-period except during the storm event from 12:00 5 May to 00:00 6 May 2013 (from Chu et al. 2021).

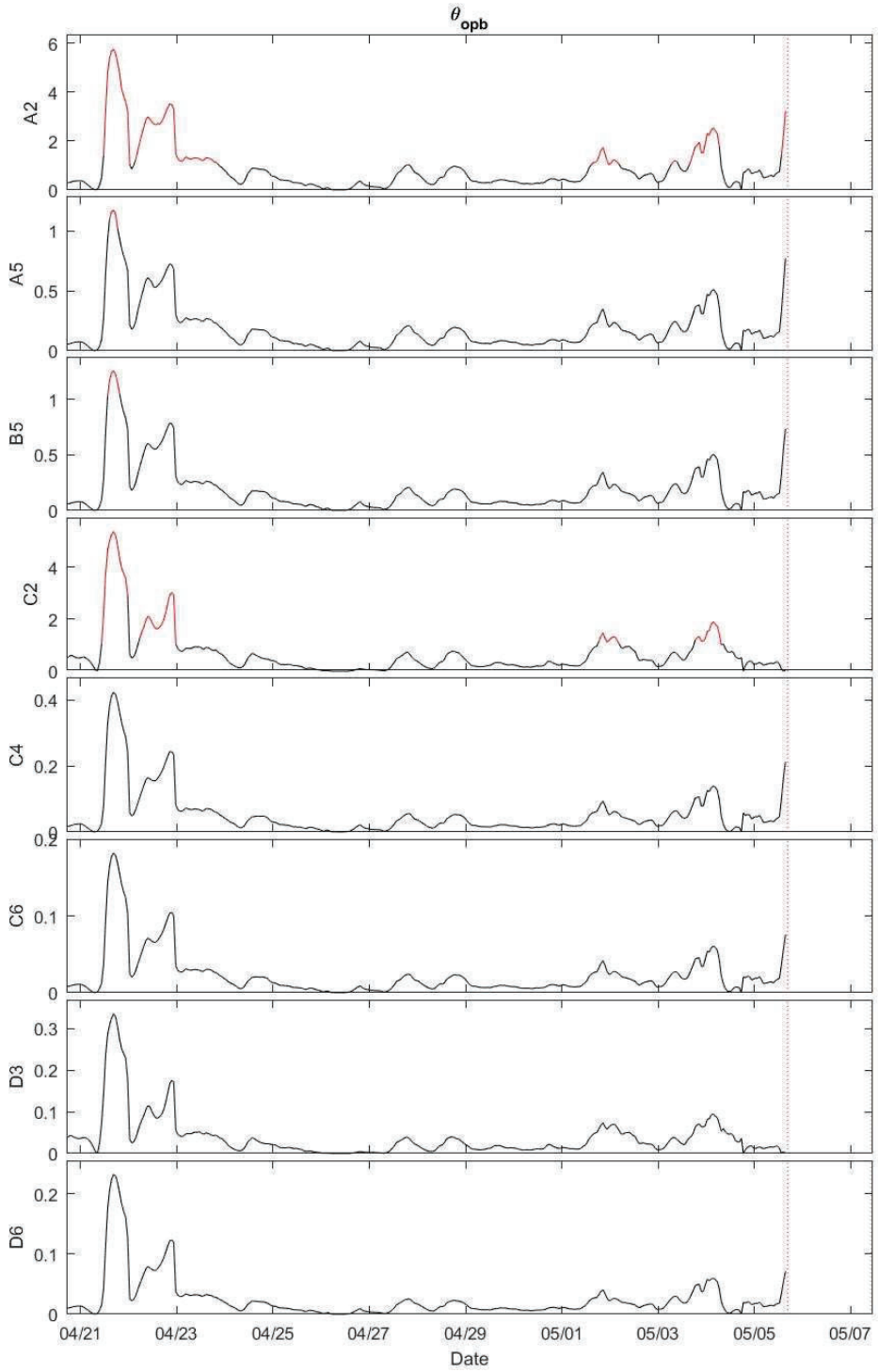

Figure 30. Model predicted munitions' mobility parameters for percentage burial (θ_{opb}) at the shallow quadpod from 20 April to 7 May 2013. The red color shows that the condition for rolling the object [θ_{opb}>1] is satisfied. The parameters θ_{opb} is not computed between 12:00 5 May to 00:00 6 May 2013 since the predicted burial percentage $p_B(t)$ is larger than 0.5. Among the eight objects, only A2 and C2 have evident time periods that the condition for rolling the object [θ_{opb}>1] is satisfied (from Chu et al. 2021).

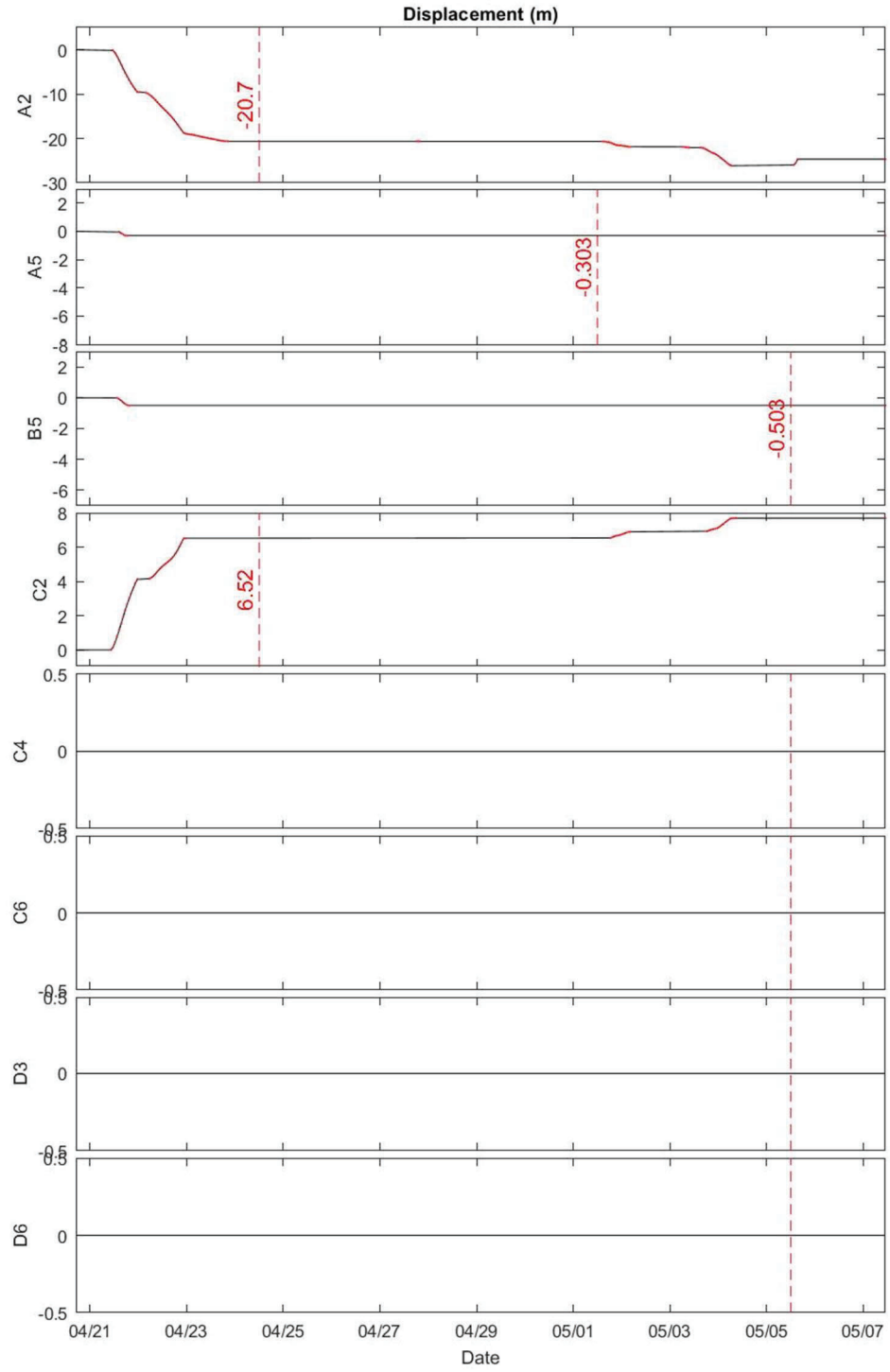

Figure 31. Model predicted displacement $l(t)$ for each munition at the shallow quadpod from 20 April to 7 May 2013. Among the eight objects, only A2 and C2 were immediately mobile and displaced 20.7 m (A2) and 6.52 m (C2) on 12:00 24 April 2013 (dashed line); other munitions A5, B5, C4, C6, D3, D6 were completely motionless. According to the TREX13 report (Calantoni et al. 2014), the objects A2 and C2 were immediately mobile and transported out of the field of view because they were last seen on 23 April 2013. After 23 April 2013, their locations have never been observed (from Chu et al. 2021).

The surrogate and replica munitions' mobility and burial were observed by divers and sector scanning sonar images during the field experiment depicted in Section 2 and in Calantoni et al. (2014). A total of 8 munitions in place at the shallow quadpod location were recovered by divers during the maintenance dive performed on 8 May 2013 (Figure 3b). Note that the munitions excavated by the divers at the shallow quadpod location on 8 May 2013 were immediately redeployed for the duration of the experiment. An overview of the observed munitions' mobility throughout the whole TREX13 experiment (20 April to 07 May 2013) is shown in Figure 32a, and during the storm event on 13:00-20:00 5 May 2013 in Figure 32b. The objects A2 and C2 were immediately mobile and transported out of the field of view because they were last seen on 23 April 2013 (very crude observational information). However, the other objects were almost not mobile (Figure 32a). The predicted large displacements of 20.7 m of A2 from12:00 21 April to 12:00 24 April 2013 and
6.52 m for C2 from 12:00 21 April to 00:00 23 April 2013 (Figure 31) qualitatively agree with the crude observational information about on A2 and C2. Furthermore, overview of the modeled munition' mobility throughout the whole TREX13 experiment (20 April to 07 May 2013) is shown in Figure 32c, and during the storm event on 13:00-20:00 5 May 2013 in Figure 32d. Similarity between the observation (Figures. 32a, b) and the model prediction (Figures. 32 c, d) shows model capability.

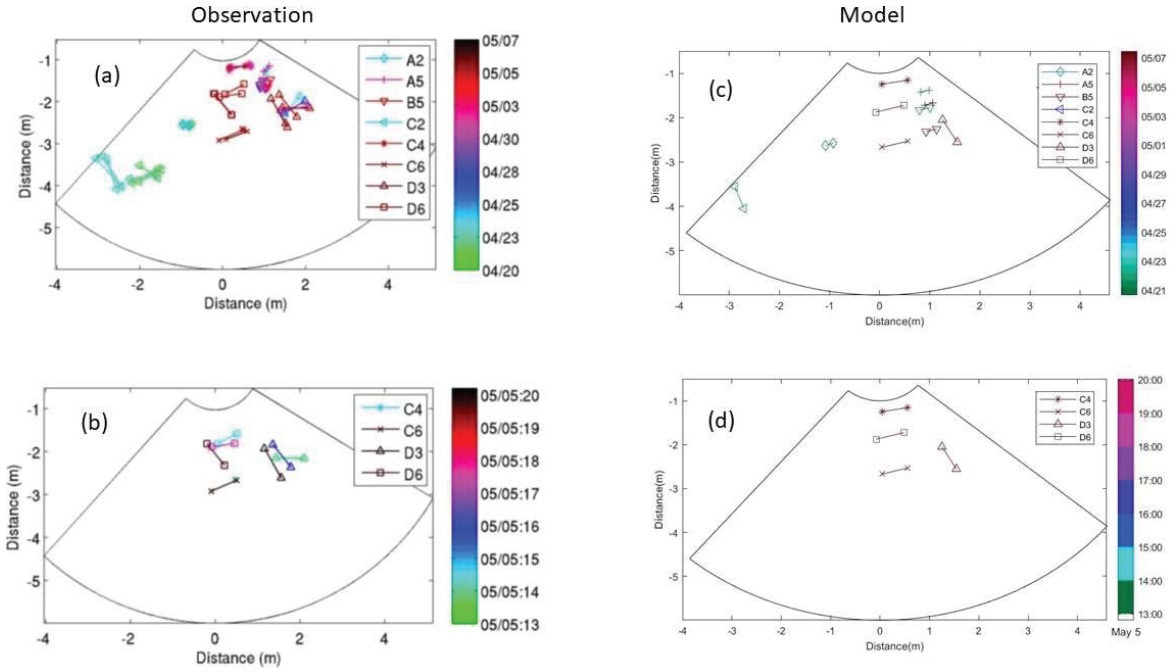

Figure 32. Positions for all visible munitions at the shallow quadpod location up to the maintenance diver performed on 8 May: (a) observation for 20 April – 07 May 2013, (b) observation for 13:00-20:00 on 5 May 2013, (c) model prediction for 20 April – 07 May 2013, and (d) model prediction for 13:00-20:00 on 5 May 2013. Note that Figures. 32a and 32b were copied from Calantoni et al. (2014). The color bars denote the last time when each object was visible with dates for (a), (c) and hour on 5 May for (b) (d) (from Chu et al. 2021).

5. Products

5.1. MS and PhD Theses

The project supports Dr/LCDR Vinicius S. Pessanha for completing his graduate studies:

(a) Vinicius S. Pessanha: Modeling of morphological responses to storm event during TREX13 experiment. MS Thesis, Physical Oceanography, Naval Postgraduate School, pp.55, December 2019.
(b) Vinicius S. Pessanha: Seabed morphological prediction with application to mobility and burial of munitions. PhD Dissertation, Physical Oceanography, Naval Postgraduate School, pp.129, December 2022.

5.2. Postdoctoral Research

The project supports Dr. Matt Gough for his postdoctoral research from 2019-2022.

5.3. Six Peer Reviewed Publications:

(a) Pessanha, V.S., P.C. Chu, M.K., Gough, and M.M. Orescanin, 2023a: Sand wave migration near the southeastern corner of Martha's Vineyard, Massachusetts, USA. *International Journal of Sediment Research*, **38**, https://doi.org/10.1016/j.ijsrc.2023.04.006
(b) Pessanha, V.S., P.C. Chu, M.K., Gough, and M.M. Orescanin, 2023b: Coupled model to predict wave-induced liquefaction and morphological changes. *Journal of Sea Research*, **192**, https://www.sciencedirect.com/science/article/pii/S1385110123000187?via%3Dihub.
(c) Chu, P.C., C.W. Fan, J. Calantoni, and A. Sheremet, 2022: Prediction of mobility and burial of objects on sandy seafloor. *IEEE Journal of Oceanic Engineering*, **47**, No. 1, January 2022. https://ieeexplore.ieee.org/stamp/stamp.jsp?arnumber=9552391&tag=1
(d) Gough, M.K., P.C. Chu, Pessanha, V.S., and J. Calantoni, 2022: Deep burial of a tapered cylinder by an energetic wave event. *IEEE Journal of Oceanic Engineering*, **47**, https://ieeexplore.ieee.org/document/9976217
(e) Pessanha, V.S., P.C. Chu, and M.K. Gough, 2022: Sediment accretion in a lower-energetic location during two consecutive cold fronts. *Journal of Operational Oceanography*, http://doi.org/10.1080/1755876X.2022.2100145
(f) Chu, P.C., V.S. Pessanha, C.W. Fan, and J. Calantoni, 2021: Coupled Delft3D-object model to predict mobility of munition on sandy seafloor. *Fluids*, **6** (9), 330, https://doi.org/10.3390/fluids6090330.

5.4. Establishment of Coupled Delft3D-UnMUMB Model

Coupled Delft3D-Underwater Munition Mobility and Burial (UnMUMB) Model has been developed with the User's Guide, https://apps.dtic.mil/sti/trecms/pdf/AD1173688.pdf

6. Conclusions and Implication for Future Research

The following points summarize this report.

A coupled Delft3D-UnMUMB model was established to predict munition's mobility and burial on sandy seafloor. The Delft3D model is used to predict seabed environment such as currents, waves (peak wave period, significant wave height, wave direction), water level, sediment transport, and seabed change, which are taken as the forcing term to the object model consisting of three components: (a) object's physical parameters such as diameter, length, mass, and rolling moment, (b) dynamics of rolling cylinder around its major axis, and (c) empirical sediment scour model with re-exposure parameterization. The model is compared with the observational data collected from a field experiment from 21 April to 13 May 2013 off the coast of Panama City, Florida funded by the DoD SERDP Program, i.e., MR-2320. The experimental data contains both munitions' mobility using sector scanning sonars and maintenance divers as well as simultaneous environmental time series data of the boundary layer hydrodynamics and sediment transport conditions. Comparison between modeled and observed data clearly shows the model capability.

Burial evolution of surrogate munition D6 (with diameter D) after deep localized scouring was identified with sonar imagery during an energetic wave event off the coast of Panama City, Florida in TREX13 (i.e., SERDP MR-2320). The evolving scour depth (S) during the burial was estimated from geometric techniques using the angle of repose of the sandy sediment applied to the sonar shadow extending from the cylinder. Power law relationships for the scour-induced equilibrium burial depth of the cylinder (S_{eq}) as functions of the Shields (θ) parameter and Keulegan-Carpenter (KC) number, and $\theta \cdot KC$ were determined from observed S/D during the wave event. S_{eq} relationships from previous studies using θ, KC, and $\theta \cdot KC$ determined with the stochastic approach, increased S_{eq} by 20-65% and improved comparisons with S_{eq} derived from the wave event suggesting that the largest waves modulate scour and burial. In these comparisons there was good agreement with S_{eq} as a function of θ although S_{eq} as functions of KC and $\theta \cdot KC$ continued to be under-predicted by previous studies. Majority of previous studies were performed in controlled laboratory environments with exception of one study where S_{eq} as a function of KC was found to be consistent with S_{eq} during the wave event implying laboratory experiments may

underestimate S_{eq} when compared to random wave environments.

A coupled Delft3D and wave-induced liquefaction model was developed to predict morphological changes and seafloor instability. The Delft3D model was employed to predict water level, currents, waves, and seafloor evolution and provide the forcing term to the wave-induced liquefaction model. The model was validated using observations from instrumentation attached to two quadpods moored at the 7.5 and 20 m bathymetric contours in TREX13 off the coast of Panama City, Florida. The field data include seafloor elevation relative to the instrumentation at the shallow quadpod, obtained from pencil beam sonar observations, and the maximum backscatter from the pulse coherent acoustic Doppler profiler. Observations determined that the seafloor elevated by 0.05 m during the first wave event and by a previously observed 0.1–0.15 m during the second wave event. By comparing the water level observed by a nearby NOAA tide station, it is determined that the 0.05 m seafloor elevation increase during the first wave event is attributed to sediment accretion, whereas the 0.1–0.15 m elevation increase during the second wave event is attributed to settling of the shallow quadpod into the sandy seafloor. The coupled model output is used to build maps of liquefaction degree and estimated failure depth. Results indicate liquefaction occurred in areas with depth/wavelength ratios smaller than 0.25, which is consistent with a previously observed sinking of the shallow quadpod sank during the second wave event. Model output also indicates a seafloor elevation of up to 0.05 m, suggesting that both liquefaction and sedimentation occurred near the shallow quadpod.

Sand waves of approximately 2 m in height were observed in field experiment in SERDP MR- 2319 to migrate nearly 40 m with counterclockwise rotation between two bathymetric surveys performed three months apart near the southeastern corner of Martha's Vineyard, Massachusetts. The region is characterized by strong tidal currents, intermittent energetic surface wave events, and shallow water with local depth ranging from 2 to 7 m. This study uses the process-based model, Delft3D, with a three-dimensional approach to examine the sand wave dynamics by incorporating surface waves, winds, currents, and bathymetric observations. The model successfully simulates sand wave migration in comparison to observations. Model sensitivity analyses show that the sand wave migration reduces by 65% with the absence of the surface waves. The modeled sand wave migration speed is correlated with the tidal current Shields parameter, and sharp increases in migration speed occur when the wave-driven Shields parameter increases in response to energetic surface wave events. The combined effect of tides, surface waves, and bathymetry is the origin of the rotational aspect of the sand wave, using the Shields parameter as an indicator of tidal currents and surface wave influence on sand wave dynamics.

The UnMUMB model uses the 6-DoF moment of momentum equation to predict underwater munition 's burial and mobility with various object parameters and initial conditions. The mobility is predicted by equation (13) and the burial is forecasted by equation (21). Delft3D output provides the environmental parameters around the munition, which are required by the UnMUMB model for predicting the munition's burial and mobility. The capability of the coupled Delft3D-UnMUMB model was vilified using environmental conditions and spanning a range of object parameters reported in a separate study (MR-2320). The surrogate and replica munitions' mobility and burial were observed by divers and sector scanning sonar images during the field experiment depicted in Section 2 and in Calantoni et al. (2014). A total of 8 munitions in place at the shallow quadpod location were recovered by divers during the maintenance dive performed on 8 May 2013

(Figure 3b). Among 8 munitions, the 4 munitions with relative density (ρ_o/ρ_w) larger than 2.5, i.e., 3.11 (C4), 7.19 (C6), 2.72 (D3), and 7.19 (D6). The coupled UnMUMB-Delft3D model predicted no motion for C4 (ρ_o/ρ_w=3.11), C6 (ρ_o/ρ_w=7.19), D3 (ρ_o/ρ_w=2.72), and D6 (ρ_o/ρ_w=7.19); and mobility with displacement of 20.7 m for A2 (ρ_o/ρ_w=1.43), 6.52 m for C2 (ρ_o/ρ_w=1.20), 0.50 m for B5 (ρ_o/ρ_w=2.36), and 0.30 m for A5 (ρ_o/ρ_w=2.60). This may partially answer the question raised by Traykovski and Austin (2017) in a separate study (MR-2319): "For instance, would rapidly increasing waves be able to mobilize objects with relative densities greater than 2.5?" Future work should explore the role to determine the threshold for mobility with objects near to or less dense than water-saturated sand tended to migrate, and denser objects tended to bury; and to identify munition 's migration distance under energetic wave and current forcing in environment with bathymetric constrained and with no bathymetric constrained. Besides, for operational use in the real world, the geometrical characteristics of objects need to be upgraded to include various shapes fitting the real munitions.

Literature Cited

Bennett, R.H., 2000: Mine Burial Prediction Workshop Report and Recommendations, Final Report prepared for ONR Dr. R.H. Wilkens, Dr. J. H. Kravitz, and Dr. D. G. Toderoff, Seaprobe, Inc., *Technical Report Number SI-0000-02*, pp 21.

Booij, N., R.C. Ris, & L.H. Holthuijsen, 1999: A third-generation wave model for coastal regions: 1. Model description and validation. *Journal of Geophysical Research,* **104**, 7649–7666.

Calantoni, J., T. Staples, & A. Sheremet, 2014: Interim Report - *Long Time Series Measurements of Munitions Mobility in the Wave-Current Boundary Layer*. **SERDP MR-2320**, 1- 48.

Campmans, G. H. P., P. C. Roos, H. J. de Vriend, & S. J. M. H. Hulscher, 2018: The Influence of Storms on Sand Wave Evolution: A Nonlinear Idealized Modeling Approach. *Journal of Geophysical Research,* **123**, 2070–2086. https://doi.org/10.1029/2018JF004616

Cataño-Lopera, Y.A., S.T. Demir, & M.H. García, 2007: Self-burial of short cylinders under oscillatory flows and combined waves plus current. *IEEE Journal of Oceanic Engineering*, **32**, 191–203.

Chu, P.C., 2009: Mine impact burial prediction from one to three dimensions. *Applied Mechanics Review*, **62**, no. 1, 010802, 1-25.

Chu, P.C., 2020: Interim Report - *Coupled Ensemble Seafloor Environment and 6-DOF Model for Assessing Characteristics of Munitions Underwater and Their Environment*, **SERDP MR19-C1-1073**, 1-52, https://apps.dtic.mil/sti/pdfs/AD1135276.pdf

Chu, P.C., & C.W. Fan, 2022: *User Guide – Coupled Delft3D-Underwater Munition Scour Burial Model*, **SERDP MR19-C1-1073**,1-70, https://apps.dtic.mil/sti/trecms/pdf/AD1173688.pdf

Chu, P.C., C.W. Fan, A.D. Evans, & A.F. Gilles, 2004: Triple coordinate transforms for prediction of falling cylinder through the water column. *Journal of Applied Mechanics*, **71**, 292-298.

Chu, P.C., A.F. Gilles, & C.W. Fan, 2005: Experiment of falling cylinder through the water column. *Experimental and Thermal Fluid Sciences*, **29**, 555–568.

Chu, P.C., & C.W. Fan, 2005: Pseudo-cylinder parameterization for mine impact burial prediction. *Journal of Fluids Engineering*, **127**, 1,515-1,520.

Chu, P.C., & C.W. Fan, 2006: Prediction of falling cylinder through air-water-sediment columns. *Journal of Applied Mechanics*, **73**, 300-314.

Chu, P.C., & C.W. Fan, 2007: Mine impact burial model (IMPACT35) verification and improvement using sediment bearing factor method. *IEEE Journal of Oceanic Engineering*, **32**, 34-48.

Chu, P.C., C.W. Fan, J. Calantoni, & A. Sheremet, 2022: Prediction of mobility and burial of objects on sandy seafloor. *IEEE Journal of Oceanic Engineering*, **47**, No. 1, January 2022. https://ieeexplore.ieee.org/stamp/stamp.jsp?arnumber=9552391&tag=1

Chu, P.C., V.S. Pessanha, C.W. Fan, & J. Calantoni, 2021: Coupled Delft3D-object model to predict mobility of munition on sandy seafloor. *Fluids*, **6** (9), 330, https://doi.org/10.3390/fluids6090330.

Deltares, 2019a: Delft3D-Flow—Simulation of multi-dimensional hydrodynamic flows and transport phenomena, including sediments, User Manual. https://content.oss.deltares.nl/delft3d/manuals/Delft3D-FLOW_User_Manual.pdf.

Deltares, 2019b: Delft3D-Wave—Simulation of short-crested waves with SWAN, User Manual. https://content.oss.deltares.nl/delft3d/manuals/Delft3D-WAVE_User_Manual.

Demir, S.T., & M.H. García, 2007: Experimental studies on Burial of finite length cylinders under oscillatory flow. *Journal of Waterway, Port, Coastal and Ocean Engineering* ASCE, **133** (2), 117–124.

Donas, A., I. Famelis, P.C. Chu, & G. Galanis, 2021: Optimization of the Navy's three-dimensional mine impact burial prediction simulation model, IMPACT35, using high-order numerical models. *Journal of Defense Modeling and Simulation: Application, Methodology, Technology* 1-15, doi: 10.1177/15485129212921102866l.

Donelan, M.A., J. Hamilton, & W.H. Hui, 1985: Directional spectra for wind-generated waves. *Philosophical Transactions of Royal Society London*, A **315**L, 509–562.

Fang, H.W., & W. Rodi, 2003: Three-dimensional calculations of flow and suspended sediment transport in the neighborhood of the dam for the three gorges project (TGP) reservoir in the Yangtze River. *Journal of Hydraulic Research*, **41**, 379-394.

Fang, H.W., & G.Q. Wang, 2000: Three-dimensional mathematical model of suspended-sediment transport. *Journal of Hydraulic Engineering*, **126**, 578-592.

Friedrichs, C.T., S.E. Rennie, & A. Brandt, 2016: Simple parameterized models for predicting mobility, burial and re-exposure of underwater munitions. Final Report, US Strategic

Environmental Research and Development Program, Project MR-2224, 1- 68.

Gough, M.K., P.C. Chu, V.S. Pessanha, & J. Calantoni, 2022: Deep burial of a tapered cylinder by an energetic wave event. *IEEE Journal of Oceanic Engineering*, **47**, IEEE Xplore.ieee.org/stamp/stamp.jsp?tp=&arnumber=9976217

Hasselmann, K.F., T.P. Barnett, E. Bouws, H.C. Carlson, D.E. Cartwright, K. Enke, J.A. Ewing, H. Gienapp, D. E. Hasselmann, P. Kruseman, A. Meerburg, P.M. Müller, D. J. Olbers, K. Richter, W. Sell, & H. Walden, 1973:. Measurements of wind-wave growth and swell decay during the Joint North Sea Wave Project (JONSWAP). *Ergaenzungsheft zur Deutschen Hydrographischen Zeitschrift, Reihe A*, 8,1–95.

Hopkins, J., S. Elgar, & B. Raubenheimer, 2017: Flow separation effects on shoreline sedimenttransport. *Coastal Engineering*, **125**, 23–27, https://doi.org/10.1016/j.coastaleng.2017.04.007

Hsu, J. R. C., & D. S. Jeng, 1994: Wave-induced soil response in an unsaturated anisotropic seabed of finite thickness. *International Journal for Numerical and Analytical Methods in Geomechanics*, **18**, 785–807.

Jeng, D. S., 2018: *Mechanics of Wave-Seabed-Structure Interactions*. *Mechanics of Wave-Seabed-Structure Interactions*. https://doi.org/10.1017/9781316672266

Jia, Y., L. Zhang, J. Zheng, X. Liu, D. S. Jeng, & H. Shan, 2014: Effects of wave-induced seabed liquefaction on sediment re-suspension in the Yellow River Delta. *Ocean Engineering*, **89**, 146–156. https://doi.org/https://doi.org/10.1016/j.oceaneng.2014.08.004

Jones, K. R., & P. Traykovski, 2019: Interaction of Superimposed Megaripples and Dunes in a Tidally Energetic Environment. *Journal of Coastal Research*, **35**, 948–958. https://doi.org/10.2112/JCOASTRES-D-18-00084.1

Kamke, E., 1977: *Differentialgleichungen: Losungsmethoden und Losungen, I, Gewohnliche Differentialgleichungen*, B. G. Teubner, Leipzig.

Kimball, P., J. Bailey, S. Das, R. Geyer, T. Harrison, C. Kunz, et al., 2015: The WHOI Jetyak: An autonomous surface vehicle for oceanographic research in shallow or dangerous waters. In *2014 IEEE/OES Autonomous Underwater Vehicles, AUV 2014*. https://doi.org/10.1109/AUV.2014.7054430

Klammler, H., A. Sheremet, & J. Calantoni, 2020: Seafloor Burial of Surrogate Unexploded Ordnance by Wave-Induced Sediment Instability. *IEEE Journal of Oceanic Engineering*, **45**, 927–936. https://doi.org/10.1109/JOE.2019.2919356

Krause, P., D. Boyle, & F. Bäse, 2005: Comparison of Different Efficiency Criteria for Hydrologic Models. *Advances in Geosciences*. **5**. https://doi.org/10.5194/adgeo-5-89-2005.

Li, Z. & P. D. Komar, 1986: Laboratory measurements of pivoting angles for applications to selective entrainment of gravel in a current. Sedimentology, **33**, 413- 423.

https://doi.org/10.1111/j.1365-3091.1986.tb00545.x.

Nielsen, P., 1992: *Coastal Bottom Boundary Layers and Sediment Transport*. Advanced Series on Ocean Engineering 4. World Scientific, Singapore, pp.324.

Penko, A. M., J. Calantoni, & B. T. Hefner, 2017: Modeling and observations of sand ripple formation and evolution during TREX13. IEEE *Journal of Oceanic Engineering*, **42**, 260–267. https://doi.org/10.1109/joe.2016.2622458

Pessanha, V. S., 2019: *Modeling of Morphological Responses to a Storm Event During TREX13*. Master Thesis, Department of Oceanography, Naval Postgraduate School, pp.55, December 2019 (Sponsor: SERDP, Thesis Adviser: P.C. Chu).

Pessanha, V. S., 2022: *Seabed Morphological Prediction with Application to Mobility and Burial of Munitions*. PhD Dissertation, Department of Oceanography, Naval Postgraduate School, pp.55, December 2022 (Sponsor: SERDP, Dissertation Adviser: P.C. Chu).

Pessanha, V.S., P.C. Chu, & M.K. Gough, 2022: Sediment accretion in a lower-energetic location during two consecutive cold fronts. *Journal of Operational Oceanography*, http://doi.org/10.1080/1755876X.2022.2100145

Pessanha, V.S., P.C. Chu, M.K., Gough, and M.M. Orescanin, 2023a: Coupled model to predict wave-induced liquefaction and morphological changes. *Journal of Sea Research*, **192**, https://www.sciencedirect.com/science/article/pii/S1385110123000187?via%3Di hub.

Pessanha, V.S., P.C. Chu, M.K., Gough, and M.M. Orescanin, 2023b: Sand wave migration near the southeastern corner of Martha's Vineyard, Massachusetts, USA. *International Journal of Sediment Research*, **38**, https://doi.org/10.1016/j.ijsrc.2023.04.006

Rennie, S.E., 2017: Final Report - *Underwater Munitions Expert System to Predict Mobility and Burial*. **SERDP MR-2227**, 1-38.

Rennie, S.E., A. Brandt, & C.T. Friedrichs, 2017: Initiation of motion and scour burial of objects underwater, *Ocean Engineering*, **131**, 282-294.

Roelvink, D. J. A. & D. J. Walstra, 2005: Keeping it simple by using complex models. *Advances in Hydroscience and Engineering*, **6**, 1-11.

SERDP, 2010: "Munitions in the Underwater Environment: State of the Science and Knowledge Gaps," White Paper (https://www.serdp-estcp.org/Featured-Initiatives/Munitions-Response-Initiatives/Munitions-in-the-Underwater-Environment).

Shields, A., 1936: Application of Similarity Principles and Turbulence Research to Bed-load Movement (translated version). *Hydrodynamics Laboratory*, **167**.

Soulsby, R.L., 1987: Calculating bottom orbital velocity beneath waves. *Coastal Engineering*, **11**, 371–380.

Sumer, B.M., C. Truelsen, T. Sichmann, & J. Fredsøe, 2001: Onset of scour below pipelines and

self-burial. *Coastal Engineering*, **42**, 313–335.

Taber, V.L., 1999: Environmental Sensitivity Study on Mine Impact Burial Prediction Model. Master Thesis, Department of Oceanography, Naval Postgraduate School, pp. 50, March 1999 (Sponsor: ONR, Thesis Adviser: P.C. Chu).

Tonnon, P. K., L. C. van Rijn, & D. J. R. Walstra, 2007: The morphodynamic modelling of tidal sand waves on the shoreface. *Coastal Engineering*, **54**, 279–296. https://doi.org/10.1016/j.coastaleng.2006.08.005

Traykovski, P., M.D. Richardson, L.A. Mayer, & J.D. Irish, 2007: Mine burial experiments at the Martha's vineyard coastal observatory. *IEEE Journal of Oceanic Engineering*, **32**, 150-166.

Traykovski, P., & T. Austin, 2017: Final Report - *Continuous Monitoring of Mobility, Burial, and Re-exposure of Underwater Munitions in Energetic Near-shore Environments*., **SERDP MR-2319**, 1- 44.

Trembanis, A.C., C.T. Friedrichs, M.D. Richardson, P. Traykovski, P. A. Howd, P.A. Elmore, P.A., & T. F. Wever, 2007: Predicting seabed burial of cylinders by wave-induced scour: application to the sandy inner shelf off Florida and Massachusetts. *IEEE Journal of Oceanic Engineering*, **32**, 167–183.

van Rijn, L. C., 1993: *Principles of Sediment Transport in Rivers, Estuaries and Coastal Seas*, Aqua Publications, 1-654.

van Rijn, L.C., D. Walstra, B. Grasmeijer, J. Sutherland, S. Pan, & J. Sierra, 2003: The predictability of cross-shore bed evolution of sandy beaches at the time scale of storms and seasons using process-based Profile models. *Coastal Engineering*, **47**(3), 295–327.

Voropayev, S. I., F.Y. Testik, H.J.S. Fernando, & D.L. Boyer, 2003: Burial and scour around short cylinder under progressive shoaling waves. *Ocean Engineering*, **30**: 1647-1667.

Walden, 1973: *Measurements of Wind-Wave Growth and Swell Decay during the Joint North Sea Wave Project (JONSWAP)*, Deutsche Hydrographisches Institut, Hamburg, Suppl. A 8 (12), 1- 95.

Wang, Z., B. Liang, G. Wu, & B. W. Borsje, 2019: Modeling the formation and migration of sand waves: The role of tidal forcing, sediment size and bed slope effects. *Continental Shelf Research*, **190**. https://doi.org/10.1016/j.csr.2019.103986

Whitehouse, R., 1998: *Scour at Marine Structures: a Manual for Practical Applications*. Thomas Telford Publications, London, 1-198.

Wiberg, P.L., & C.R. Sherwood, 2008: Calculating wave-generated bottom orbital velocities from surface wave parameters. *Computers and Geosciences*, **34**, 1,243-1,262.

Willmott, C.J., 1981: On the Validation of Models. *Physical Geography*, **2**, 184-194.